Free vibration analysis of curved metallic and composite beam structures using a novel variable-kinematic DQ method

Free vibration analysis of curved metallic and composite beam structures using a novel variable-kinematic DQ method

Yang Yan[a*], Erasmo Carrera[b,c†], Alfonso Pagani[b‡]

[a] *The Solid Mechanics Research Center, Beihang University, 100191 Beijing, China*

[b] *Mul^2, Department of Mechanical and Aerospace Engineering, Politecnico di Torino, Corso Duca degli Abruzzi 24, 10129 Torino, Italy*

[c] *Department of Mechanical Engineering, College of Engineering, Prince Mohammad Bin Fahd University P.O. Box 1664, Al Khobar 31952, Kingdom of Saudi Arabia*

Submitted to

Mechanics of Advanced Materials and Structures

Author for correspondence:
Alfonso Pagani,
Department of Mechanical and Aerospace Engineering,
Politecnico di Torino,
Corso Duca degli Abruzzi 24,
10129 Torino, Italy,
tel: +39 011 090 6887,
fax: +39 011 090 6899,
e-mail: alfonso.pagani@polito.it

[*] Postdoctor, e-mail: yanyang864914630@126.com
[†] Professor of Aerospace Structures and Aeroelasticity, e-mail: erasmo.carrera@polito.it
[‡] Associate Professor, e-mail: alfonso.pagani@polito.it

ABSTRACT

The present paper investigates the 3D free vibration behavior of curved metallic and composite beams via a novel beam theory. The refined beam theory is constructed within the framework of the Carrera Unified Formulation (CUF), which expands 3D displacement fields as 1D generalized displacement unknowns over the cross-section. As a novelty, a set of improved hierarchical Legendre polynomials called the improved hierarchical Legendre expansion (IHLE) is used to describe the cross-sectional deformation. In this way, displacements at shared sides between piles can be interpolated by Lagrange polynomials, while displacements at the rest of the cross-section remain to be defined by hierarchical Legendre polynomials. Such determined cross-sectional kinematics not only retain the hierarchical properties of HLE in part but also facilitate the implementation of the Layer-Wise approach without paying much attention to the order that expansion terms appear over the cross-section. Due to the absence of the mesh generation and the convenience of collocation techniques, the differential quadrature based-meshless method is employed for the approximate solution of strong form governing equations derived by the principle of virtual displacements. Several numerical cases, including curved beams with various material properties and boundary conditions, are proposed to illustrate the optimized computational efficiency of this novel model over the 3D finite element method and consistent convergence properties over the previous CUF-HLE model.

Keywords: Differential quadrature method; Carrera Unified Formulation; Free vibration; Curved beams; Improved hierarchical Legendre expansions

1 Introduction

Composite materials as an alternative to metallic counterparts have gained much attention owing to their enhanced capability to tailor the structural behavior for specific purposes. In practical engineering applications, these materials are widely used to create laminated structures, such as beams, plates and shells, which are subsequently assembled into primary and secondary components of the aeronautical industry, such as rotor blades of helicopters or stiffeners of wing panels, to name a few [1]. Generally speaking, composite beams are often constructed with a straight or curved axis and a rectangular or thin-walled cross-section. Compared to straight beams, the incorporation of axial curvature increases structural stiffness, together with the complex axial-bending-torsional coupling effect [2]. Accordingly, a refined analysis model is indispensable for a better understanding of mechanical behaviors of curved beams, e.g. vibration behaviors.

The investigation that falls into the spectrum of the curved metallic beam is reported below. Chidamparam and Leissa [3] made an exhaustive review of published papers on the in-plane, out-of-plane, and coupled vibrations of curved bars, beams, rings, and arches for a variety of shapes. Yu and Nie [4] derived analytical formulae for calculating shearing and radial stresses based on a Volterra integral equation of the second kind. The differential quadrature element method (DQEM) was employed by Chen [5] for the in-plane vibration analysis of curved beam structures. Kang et al. [6] proposed harmonic wave solutions for free vibration analysis of planar curved beams with general support conditions.

As for research about the curved composite beam, Hajianmaleki and Qatu [7] presented an eminent review of the vibration analysis of composite beams with straight and curved axes included. In [7], the primary concern can be classified into the following aspects: the theory being applied, e.g. Equivalent Single Layer (ESL) and Layer-Wise (LW) theories; the treatment of various numerical methods for solving governing equations, e.g. finite element method (FEM), Differential transform method (DTM); experiment investigations; smart beams; and other complex effects in both materials and structures. A brief review of the first two aspects will be given in the rest of the introduction. The ESL theory describes the cross-sectional deformation regardless of the number of layers. In contrast, the LW theory treats the whole cross-section as the combination of every single layer and imposes the C^0-continuity requirement of displacement fields at the intra-layer interfaces, thus being computational costs dependent on the number of layers. Classical theories, such as the Euler-Bernoulli beam theory (EBBM) and the Timoshenko beam theory (TBM) and various higher-order shear deformation theories (HSDT) belong to the group of the ESL theory when no extra displacement constraints act on the interface between two adjacent layers. Ecsedi and Dluhi [8] performed static and free vibration analyses of curved beams with non-homogeneous material properties based on the EBBM. In their work, the geometrical shape of the cross-section is assumed to be symmetric. In this manner, exact natural frequencies can be obtained when the simply supported boundary condition is under consideration. Qatu and his collaborator [9, 10, 11] comprehensively and systematically investigated the 2D vibration problem of curved composite beams based on the EBBM and TBM. Three important conclusions can be drawn from their work: (i) the deepness term $(1 + z/R)$ should be integrated into the stiffness matrix when the ratio of the span length to radius is larger than 0.5 and various material couplings, e.g. bending-twisting, extension-bending, and extension-shearing coupling exist. (ii) EBBM is efficient and accurate for

the free vibration analysis of simply supported beams with cross-ply laminates. (iii) TBM can correctly detect the deflection, moment resultants, and natural frequencies of deeply curved beams with rectangular cross-sections featuring generic laminations as evident from 3D FEM solutions provided by ANSYS. Khdeir and Reddy [12] used the HSDT of the Reddy's type to study the dynamic behavior of a shallow composite arch in depth. EBBM and TBM can be obtained as special cases when some terms take the value of 0 for this HSDT, and a direct comparison between them was made in terms of natural frequencies and dynamic displacements. The 3D free vibration analysis of curved beam and circular rings was carried out by Bhimaraddi et al. [13, 14]. From their works, in-plane and out-of-plane motions can be observed through the third-order expansion of the circumferential displacement variable and the first-order expansion of the remaining two displacement counterparts. Matsunaga [15] presented a version of the HSDT derived from the Taylor expansion of in-plane displacement unknowns for free vibration and buckling analyses of composite circular arches. Similarly, Marur and Kant [16] assumed cubic variation of axial and transverse shear strain components and linear variation of the transverse normal strain component through the depth direction so that a refined model with seven degrees of freedom for each node was formulated and applied to study frequency spectrums of sandwich arches. Li and Soares [17] proposed a spectral FEM based on the exponential shear deformation theory for modal analysis of cross-ply laminated shallow arches. As for the model based on LW theories, related works are rare. Malekzadeh et al. [18] used the LW theory of the Reddy's type that corresponds to 1D Lagrange interpolation functions in the radial direction for in-plane free vibration analyses of laminated circle arches. Yasin et al. [19] obtained a Navier-type analytical solution for the LW theory based on Reddy's third-order theories for composite and sandwich curved beams having deep curvatures.

Interestingly, Carrera et al. [20] proposed a novel model called the Carrera Unified Formulation (CUF). According to CUF, 3D displacement fields can be expressed arbitrarily rich expansions of 1D generalized displacement unknowns. EBBM, TBM, and HSDT mentioned previously can be reproduced effortlessly in a hierarchical manner through the use of different expansion functions, which can be classified into four groups: the Taylor expansion (TE), the Lagrange expansion (LE), the Chebyshev expansion (CE), and the hierarchical Legendre expansion (HLE). Such four models implemented in the framework of CUF has been applied to solve various problems, which include static [21, 22, 23], dynamic [24, 25, 26], buckling [27, 28, 29], multi-field [30, 31, 32], progressive failure problems [33, 34, 35] of straight metallic and composite structures. Special attention is given to the CUF-HLE model due to its convenience in constructing ESL and LW theories. On the other hand, CUF-HLE combines the advantage of the hierarchy of higher-order terms in CUF-TE and the local description of cross-sectional kinematics in CUF-LE. However, notice that expansion terms related to side modes in HLE do not have a clear physical meaning, introducing the difficulty in the assembly of element matrix over the cross-section. In order to overcome this drawback, the present paper intends to introduce an improved HLE (IHLE) model, in which Legendre-type bases on the shared sides of sub-domains over the cross-section are transformed to Lagrange-type nodal bases. Gauss-Lobatto nodal distribution scheme is chosen to improve the matrix conditioning. Such a transform allows the description of the C^0 continuity of the displacements along the sub-domain boundary through the matrix assembly at Gauss-Lobatto nodes directly and the maintenance of the hierarchical property inside the sub-domain. The traditional HLE model should pay close attention to the nodal

numbering scheme of the expansion terms over the cross-sectional sub-domain during the matrix assembly. In fact, this idea is inspired by ideas from a weak form quadrature element method called the differential quadrature hierarchical finite element method (DQHFEM), proposed by Liu et al. [36, 37]. They proposed various plane and spatial elements within the framework of DQHFEM as a modification of the *p*-version of FEM (*p*-FEM), developed by Babuska et al. [38] and verified the advantage of convenient matrix assembly and imposition of non-homogeneous boundary conditions. Nevertheless, it is important to highlight that the aim of this paper is that the idea of the basis transformation at the intra-layer interfaces is employed to construct structural theories rather than numerical methods.

Besides, weak-form solutions sought by FEM is available in the overwhelming majority of the literature pertaining to CUF models. The achieved accuracy and efficiency scales with the number and the type of the chosen element. In contrast, an endeavor to find strong-form solutions still deserves due to the unnecessary mesh generation. Carrera et al. [39, 40, 41, 42] presented a refined Navier-type closed-form solution for the analysis of straight and curved beams. However, the only fly in the ointment is that its analysis could be limited to metallic or cross-ply laminated composite structures with simply supported boundary conditions. The other contribution to the curved composite beam accomplished by the CUF-based FEM can be seen in the literature [43]. Subsequently, Carrera's group [44, 45] and Weaver's group [46, 47] used collocation-based methods, e.g. Radial Basis Functions (RBF) and DQM for the analysis of the straight beam.

The current work intends to develop a novel beam model called CUF-IHLE and applies DQM to solve the free vibration problem of the curved spatial beam for the first time. DQM was initially proposed by Bellman et al. [48], who approximated the partial derivative of a function as a weighted sum of function values at some discretization points. High-order Lagrange basis functions are recommended to compute weighting coefficients [49]. Due to its faster convergence and spectral accuracies, DQM has been vastly employed to solve substantial structural engineering problems.

The rest of this paper is organized as follows. Initially, the geometrical relation in the Frenet-Serret framework and constitutive law are introduced in Section 2; then, the CUF kinematic field is explained in Section 3, where insights about the relationship between the HLE and IHLE are provided; the derivation of the strong-form governing equation for free vibration problems is presented in Section 4; followed by the DQ-based discrete strategy and the formulation of a linear eigenvalue system in terms of fundamental nuclei in Section 5; the potential of the proposed approach is shown in Section 6 via the consideration of curved beams composed of metallic and composite materials and being subject to various boundary conditions; finally, the main conclusions are drawn in Section 7.

2 Curved beams: geometrical and constitutive relations

In a general way, a curved spatial beam is formed with the extension of a plane cross-section along a generic curved line. In comparison of the well-known Cartesian coordinate system, the analysis of this kind of structures is more recommended by the adoption of the Frenet-Serret coordinate system, featured by an orthonormal vector basis

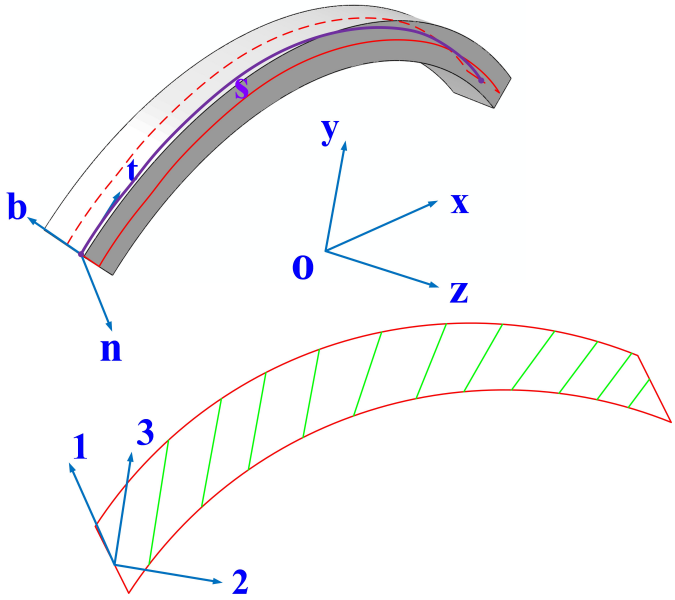

Figure 1: Coordinate system for the curved beam.

$[\boldsymbol{t}, \boldsymbol{n}, \boldsymbol{b}]$, as shown in Fig.1. In the framework of such a local reference system, the structural displacement, strain, and stress fields can be defined as:

$$\begin{aligned} \mathbf{u}(s,\xi,\eta;t) &= \left[u_s \; u_\xi \; u_\eta\right]^T \\ \boldsymbol{\varepsilon}(s,\xi,\eta;t) &= \left[\varepsilon_{\xi\xi} \; \varepsilon_{ss} \; \varepsilon_{\eta\eta} \; \varepsilon_{s\eta} \; \varepsilon_{\xi\eta} \; \varepsilon_{s\xi}\right]^T \\ \boldsymbol{\sigma}(s,\xi,\eta;t) &= \left[\sigma_{\xi\xi} \; \sigma_{ss} \; \sigma_{\eta\eta} \; \sigma_{s\eta} \; \sigma_{\xi\eta} \; \sigma_{s\xi}\right]^T \end{aligned} \tag{1}$$

where t is the time variable; $[s, \xi, \eta]$ are the coordinates of the Frenet-Serret basis. Based on the assumption of small deformations, the strain-displacement relationship is given in the following form:

$$\boldsymbol{\varepsilon} = \mathbf{D}\mathbf{u} \tag{2}$$

where $\mathbf{D}$ is the following linear differential operator matrix:

$$\mathbf{D} = \begin{bmatrix} 0 & \dfrac{\partial}{\partial\xi} & 0 \\ \dfrac{1}{H}\dfrac{\partial}{\partial s} & -\dfrac{\kappa}{H} & 0 \\ 0 & 0 & \dfrac{\partial}{\partial\eta} \\ \dfrac{\partial}{\partial\eta} & 0 & \dfrac{1}{H}\dfrac{\partial}{\partial s} \\ 0 & \dfrac{\partial}{\partial\eta} & \dfrac{\partial}{\partial\xi} \\ \dfrac{\partial}{\partial\xi} + \dfrac{\kappa}{H} & \dfrac{1}{H}\dfrac{\partial}{\partial s} & 0 \end{bmatrix} \tag{3}$$

where H equals $|1 - \kappa\xi|$ with κ being the curvature.

The material coordinate system, characterized by an orthonormal vector basis [2, 3, 1], is also shown in Fig.1. 3-axis is parallel to the fiber direction, and 2- and 1-axes represent the directions in-plane and out-of-plane perpendicular to the fibres. Consequently, the strain and stress vectors in the material coordinate system are given as:

$$\begin{aligned} \boldsymbol{\varepsilon_m} &= [\varepsilon_{33}\ \varepsilon_{22}\ \varepsilon_{11}\ \varepsilon_{21}\ \varepsilon_{31}\ \varepsilon_{23}]^T \\ \boldsymbol{\sigma_m} &= [\sigma_{33}\ \sigma_{22}\ \sigma_{11}\ \sigma_{21}\ \sigma_{31}\ \sigma_{23}]^T \end{aligned} \tag{4}$$

With regard to the orthotropic material, the 3D constitutive equation reads:

$$\boldsymbol{\sigma_m} = \mathbf{C}\boldsymbol{\varepsilon_m} \tag{5}$$

where

$$\begin{bmatrix} \sigma_{33} \\ \sigma_{22} \\ \sigma_{11} \\ \sigma_{21} \\ \sigma_{31} \\ \sigma_{23} \end{bmatrix} = \begin{bmatrix} C_{33} & C_{23} & C_{13} & 0 & 0 & 0 \\ C_{23} & C_{22} & C_{21} & 0 & 0 & 0 \\ C_{13} & C_{21} & C_{11} & 0 & 0 & 0 \\ 0 & 0 & 0 & C_{44} & 0 & 0 \\ 0 & 0 & 0 & 0 & C_{55} & 0 \\ 0 & 0 & 0 & 0 & 0 & C_{66} \end{bmatrix} \begin{bmatrix} \varepsilon_{33} \\ \varepsilon_{22} \\ \varepsilon_{11} \\ \varepsilon_{21} \\ \varepsilon_{31} \\ \varepsilon_{23} \end{bmatrix} \tag{6}$$

The explict expression of material coefficients ($C_{ij}, i, j = 1, 2, 3$) related to Young's moduli ($E_{ij}, i, j = 1, 2, 3$), shear moduli ($G_{ij}, i, j = 1, 2, 3$) and Poisson's ratio ($\nu_{ij}, i, j = 1, 2, 3$) can be found in the work of Reddy [1].

Via a coordinate transformation, the strain and stress vectors can be expressed in the Frenet-Serret coordinate system, as follows:

$$\begin{aligned} \boldsymbol{\sigma} &= \mathbf{T}\boldsymbol{\sigma_m} \\ \boldsymbol{\varepsilon} &= \mathbf{T}\boldsymbol{\varepsilon_m} \end{aligned} \tag{7}$$

where $\mathbf{T}$ is the transformation matrix, the component of which is:

$$\mathbf{T} = \begin{bmatrix} b_2^2 & a_2^2 & c_2^2 & 2a_2c_2 & 2b_2c_2 & 2a_2b_2 \\ b_1^2 & a_1^2 & c_1^2 & 2a_1c_1 & 2b_1c_1 & 2a_1b_1 \\ b_3^2 & a_3^2 & c_3^2 & 2a_3c_3 & 2b_3c_3 & 2a_3b_3 \\ b_1b_3 & a_1a_3 & c_1c_3 & a_1c_3 + a_3c_1 & b_1c_3 + b_3c_1 & a_1b_3 + a_3b_1 \\ b_2b_3 & a_2a_3 & c_2c_3 & a_2c_3 + a_3c_2 & b_2c_3 + b_3c_2 & a_2b_3 + a_3b_2 \\ b_1b_2 & a_1a_2 & c_1c_2 & a_1c_2 + a_2c_1 & b_1c_2 + b_2c_1 & a_1b_2 + a_2b_1 \end{bmatrix} \tag{8}$$

where

$$\begin{aligned} &a_1 = \cos\theta\cos\psi, && b_1 = -\sin\theta\cos\psi, && c_1 = \sin\psi \\ &a_2 = \cos\gamma\sin\theta + \cos\theta\sin\psi\sin\gamma, && b_2 = \cos\theta\cos\gamma - \sin\theta\sin\psi\sin\gamma, && c_2 = -\cos\psi\sin\gamma \\ &a_3 = \sin\gamma\sin\theta - \cos\theta\sin\psi\cos\gamma, && b_3 = \cos\theta\sin\gamma + \sin\theta\sin\psi\cos\gamma, && c_3 = \cos\psi\cos\gamma \end{aligned} \tag{9}$$

where γ, ψ and θ are the fibre orientation angles around $\boldsymbol{t}$, $\boldsymbol{n}$ and $\boldsymbol{b}$ axes.

After that, the Hooke's law can be written in the Frenet-Serret frame as

$$\boldsymbol{\sigma} = \mathbf{T}\mathbf{C}_m\mathbf{T}^T\boldsymbol{\varepsilon} = \tilde{\mathbf{C}}\boldsymbol{\varepsilon} \tag{10}$$

3 Carrera Unified Formulation (CUF)

In the light of CUF, the cross-sectional kinematics of beam-like structures are approximated by means of an expansion in terms of arbitrary functions. Accordingly, the 3D displacement field can be expressed as:

$$\mathbf{u}(s,\xi,\eta;t) = F_\tau(\xi,\eta)\mathbf{u}_\tau(s;t); \qquad \tau = 1,2,....,M \tag{11}$$

where $\mathbf{u}_\tau(s;t)$ is the generalized displacement vector, the value of which depends on s; the subscript τ indicates the summation; $F_\tau(\xi,\eta)$ is the expansion function. The developed expansion function so far can be classified into four categories: Taylor expansion (TE), Lagrange expansion (LE), Chebyshev expansion (CE), and hierarchical Legendre expansion (HLE). TE and CE describe the cross-sectional kinematics in a global sense and generally are employed to construct the Equivalent Single Layer (ESL); LE and HLE discretize the cross-section into a certain amount of local sub-domains, allowing the construction of the Layer-Wise model with ease.

3.1 Hierarchical Legendre expansion

The advantage of HLE is reported by Carrera et al. [23] who stated that it could increase the kinematic order in the local zone hierarchically, thus combining the benefits of TE, CE, and LE. However, the non-interpolative property of hierarchical Legendre bases possibly brings some difficulties to the imposition of nonhomogeneous boundary conditions and the assembly of element matrices. In order to illustrate this issue clearly, the cross-sectional expansion function composed of hierarchical Legendre polynomials will be introduced first, the expression of which is given as follows:

Vertex modes: used to describe the nodal deformation over the quadrilateral sub-domain,

$$F_\tau = \frac{1}{4}(1+\chi\chi_\tau)(1+\varsigma\varsigma_\tau); \qquad \tau = 1,2,3,4,\cdots \tag{12}$$

where χ_τ and ς_τ are the coordinates of four vertexes in the natural coordinate system. χ and ς vary within the range of [-1, +1].

Side modes: used to represent the deformation of the edge over the quadrilateral sub-domain,

$$
\begin{aligned}
F_\tau &= \frac{1}{2}(1-\varsigma)\phi_j(\chi); \qquad j \geq 2; \qquad \tau = 5, 9, 13, 18, \cdots \\
F_\tau &= \frac{1}{2}(1+\chi)\phi_j(\varsigma); \qquad j \geq 2; \qquad \tau = 6, 10, 14, 19, \cdots \\
F_\tau &= \frac{1}{2}(1+\varsigma)\phi_j(\chi); \qquad j \geq 2; \qquad \tau = 7, 11, 15, 20, \cdots \\
F_\tau &= \frac{1}{2}(1-\chi)\phi_j(\varsigma); \qquad j \geq 2; \qquad \tau = 8, 12, 16, 21, \cdots
\end{aligned}
\tag{13}
$$

where j stands for the order of the expansion function. ϕ_j is the integrated Legendre polynomial, the detailed description of which can be seen in [23].

Internal modes: used to depict the deformation inside the quadrilateral sub-domain,

$$
F_\tau = \phi_j(\chi)\phi_k(\varsigma); \qquad j,\, k \geq 2; \qquad \tau = 17, 22, 23, 28, 29, 30 \cdots \tag{14}
$$

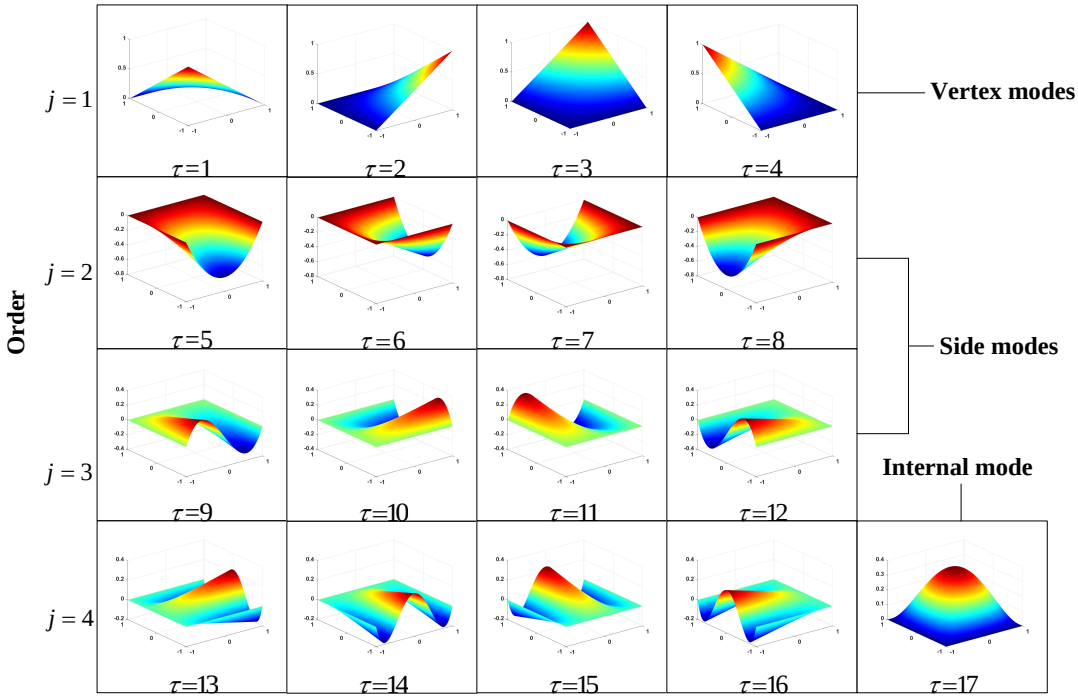

Figure 2: Hierarchical Legendre polynomials for the order from 1st to 4th.

Fig. 2 shows the HLE from order 1 to 4. It can be observed that lower-order functions are a subset of higher-order bases. Although the re-definition of lower-order functions can be avoided, such hierarchical kinematics may violate the C^0 continuity of displacements between sub-domains, since side modes do not possess the interpolative properties. Thus, displacement discontinuous phenomena will appear when the expansion terms are endowed with an inappropriate nodal numbering scheme (see Fig. 3).

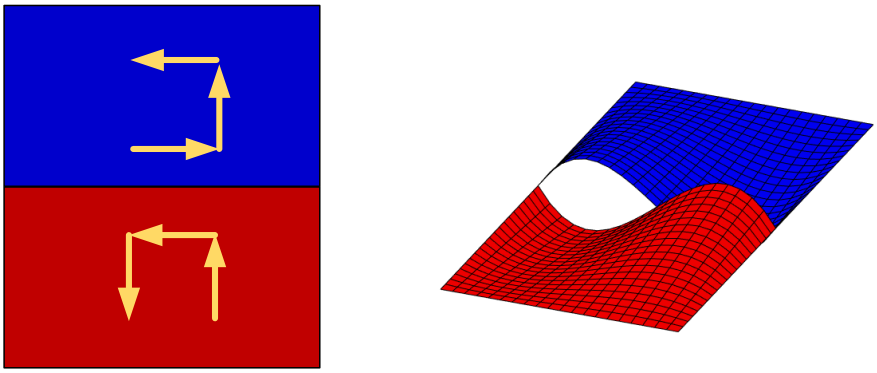

Figure 3: A kind of the nodal numbering scheme and the resulting deformation gap.

3.2 Improved hierarchical Legendre expansion

A simple alternative is the transformation of non-interpolative modes on the shared sides of sub-domains to Lagrange-type nodal bases. Such an operation leads to the improved hierarchical Legendre expansion (IHLE), which represents the main novelty of the present work.

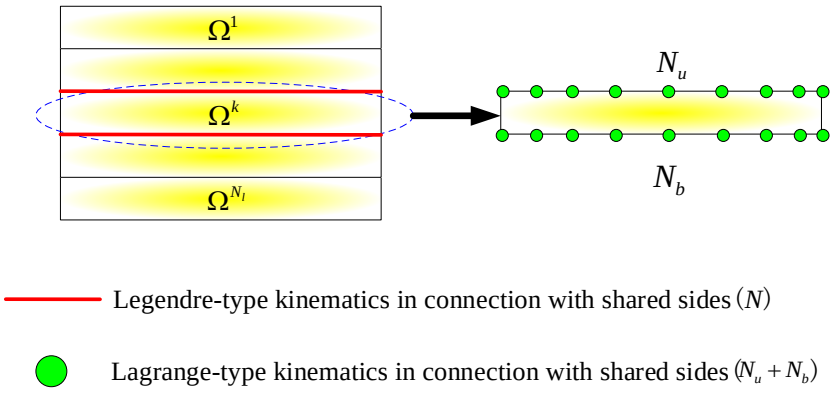

Figure 4: Transformed nodes of the kth layer of the cross-section.

Fig.4 specifies the transformed node related to the kth layer of a multi-layered curved beam, including N_u nodes in the upper line and N_b nodes in the bottom line. It should be added that the total number of transformed nodes should be equal to that of expansion terms relative to shared sides, i.e., $N_u + N_b = N$. As a result of the mathematical issue, the nodal collocation strategy is such that non-equispaced nodes, namely, Gauss-Lobatto nodes are selected for each line so that the serious oscillation phenomenon with the increasing number of nodes, referred to as Runge's phenomenon, can be weakened to some extent. If $\mathbf{u}^g(s,\xi,\eta;t) = \left[u_s^g(s,\xi,\eta;t), u_\xi^g(s,\xi,\eta;t), u_\eta^g(s,\xi,\eta;t)\right]^T$ is related to Gauss-Lobatto nodes at the cross-sectional level, the evaluation of the value for Gauss-Lobatto nodes can be expressed as:

$$\boldsymbol{U}^g = \mathbf{V}\boldsymbol{U} \tag{15}$$

where $\boldsymbol{U}^g$ is a vector, which is constructed from $\mathbf{u}^g(s,\xi,\eta;t)$; $\mathbf{V}$ is defined in a similar way; $\boldsymbol{U}$ is the vectorization

representation of $\mathbf{u}_\tau(s;t)$. The expression of these new terms is:

$$
\begin{aligned}
\boldsymbol{U}^g &= \left[u_s^g(s,\xi_1,\eta_1;t),...,u_\eta^g(s,\xi_1,\eta_1;t),...,u_s^g(s,\xi_{N_u},\eta_{N_u};t),...,u_\eta^g(s,\xi_{N_u},\eta_{N_u};t),...,u_s^g(s,\xi_N,\eta_N;t),...,u_\eta^g(s,\xi_N,\eta_N;t)\right]^T \\
\mathbf{V} &= \begin{bmatrix}
F_{Ind(1)}(\xi_1,\eta_1) & \cdots & F_{Ind(N_u)}(\xi_1,\eta_1) & \cdots & F_{Ind(N)}(\xi_1,\eta_1) \\
\cdots & \cdots & \cdots & \cdots & \cdots \\
F_{Ind(1)}(\xi_{N_u},\eta_{N_u}) & ... & F_{Ind(N_u)}(\xi_{N_u},\eta_{N_u}) & ... & F_{Ind(N)}(\xi_{N_u},\eta_{N_u}) \\
\cdots & \cdots & \cdots & \cdots & \cdots \\
F_{Ind(1)}(\xi_N,\eta_N) & ... & F_{Ind(N_u)}(\xi_N,\eta_N) & ... & F_{Ind(N)}(\xi_N,\eta_N)
\end{bmatrix} \otimes \mathbf{I} \\
\boldsymbol{U} &= \left[u_{s_{Ind(1)}}(s;t),...,u_{\eta_{Ind(1)}}(s;t),...,u_{s_{Ind(N_u)}}(s;t),...,u_{\eta_{Ind(N_u)}}(s;t),...,u_{s_{Ind(N)}}(s;t),...,u_{\eta_{Ind(N)}}(s;t)\right]^T
\end{aligned}
\tag{16}
$$

where (ξ_i,η_i) represents the coordinate of the ith Gauss-Lobatto node over the cross-section; $Ind(i)$ indicates the ith nodal numbering index; $\otimes$ stands for the Kronecker product; $\mathbf{I}$ is the 3×3 identity matrix.

Based on Eq. 15, the local displacement field related to shared sides (SS) $\mathbf{u}^{SS}(s,\xi,\eta;t)$ in the kth layer can be written as follows:

$$
\mathbf{u}^{SS} = \mathbf{G}\mathbf{V}^{-1}\boldsymbol{U}^g = L_{Ind(\tau)}(\xi,\eta)\mathbf{u}_\tau^g(s;t); \qquad \tau = 1,2,....,N \tag{17}
$$

where $\mathbf{G} = [F_{Ind(1)}, F_{Ind(2)}, ..., F_{Ind(N)}] \otimes \mathbf{I}$ is the matrix form of the expansion function $F_{Ind(\tau)}(\xi,\eta) \quad \tau = 1,2,....,N$; $\mathbf{u}_\tau^g(s;t) = \left[u_s^g(s,\xi_\tau,\eta_\tau;t), u_\xi^g(s,\xi_\tau,\eta_\tau;t), u_\eta^g(s,\xi_\tau,\eta_\tau;t)\right]^T$ refers to the generalized displacement vector of the τth Gauss-Lobatto node over the cross-section; L_τ means Lagrange-type nodal kinematics and its component can be computed via $\mathbf{G}\mathbf{V}^{-1}$.

It is worth mentioning Eq. 17 is invalid in the calculation of the displacement field for the rest of the structure. In fact, in view of Fig. 2, the side mode of each edge vanishes on other edges, whereas the internal mode vanishes on all edges. In other words, side modes of other edges and internal modes do not play any role in the displacement computation of shared sides, although they are indispensable to the versatile description of full displacement fields. Such a crucial feature offers the possibility of formulating a novel kinematic field, which states that:

$$
\begin{aligned}
\mathbf{u} &= L_{Ind(\tau_1)}(\xi,\eta)\mathbf{u}_{\tau_1}^g(s;t) + F_{\tau_2}(\xi,\eta)\mathbf{u}_{\tau_2}(s;t); \quad \tau_1 = 1,2,\ldots,N; \quad \tau_2 = 1,2,\ldots,M; \quad Ind(\tau_1) \neq \tau_2 \\
&= \bar{F}(\xi,\eta)\mathbf{u}_\tau(s;t); \quad \tau = 1,2,\ldots,M
\end{aligned}
\tag{18}
$$

where $\bar{F}(\xi,\eta)$ means the IHLE kinematics, being a mixed-mode of Lagrange and hierarchical Legendre expansions.

The main advantage of the proposed kinematic formulation is that the C^0 continuity of displacements at the intra-layer interfaces can be satisfied spontaneously without some special treatment on the nodal numbering scheme, resulting in increased efficiency in the pre-processing stage. In addition, the Lagrange expansion on the shared side can be acquired through the transformation from the hierarchical Legendre expansion directly, retaining the integrity of the input data of the original HLE model. The transformation efficiency depends on the time consumption of matrix inversion in Eq. 17.

4 Governing differential equations

For the free vibration analysis, Governing equations in the case of modal analysis can be acquired via the principle of virtual displacement (PVD), which reads,

$$\delta L_{\text{int}} + \delta L_{\text{ine}} = 0 \tag{19}$$

where δ signifies the symbol of the virtual variation; L_{int} represents the strain energy; L_{ine} is the inertial work. In detail, The strain energy takes the following integral form:

$$\delta L_{\text{int}} = \int_L \int_\Omega \delta \boldsymbol{\varepsilon}^{\mathrm{T}} \boldsymbol{\sigma} H \mathrm{d}\Omega \mathrm{d}s \tag{20}$$

where L is the arc length of the curved line; Ω means the cross-sectional area. Substitution of Eq. 2, Eq. 5 and Eq. 18 into Eq. 20, together with integration by parts, leads to the following explicit expression for the inertial work:

$$\delta L_{\text{int}} = \int_L (\delta \mathbf{u}_\tau)^{\mathrm{T}} \mathbf{K}^{\tau\zeta} \mathbf{u}_\zeta \mathrm{d}s + \left[(\delta \mathbf{u}_\tau)^{\mathrm{T}} \mathbf{\Pi}^{\tau\zeta} \mathbf{u}_\zeta\right] |_{s=0}^{s=L} \tag{21}$$

where $\mathbf{K}^{\tau\zeta}$ and $\mathbf{\Pi}^{\tau\zeta}$ are the differential stiffness matrix and matrix of natural boundary conditions with regard to 3×3 fundamental nuclei, which are invariant with respect to indexes ξ and ζ. Components of fundamental nuclei are given in Appendix A.

Accordingly, the virtual variation of the inertial work is given by the following expression:

$$\delta L_{\text{ine}} = \int_L \int_\Omega \rho \delta \mathbf{u} \ddot{\mathbf{u}} H \mathrm{d}\Omega \mathrm{d}s \tag{22}$$

where ρ is the material density; double dots over the variable represent the second derivative versus time (t). Using Eq. 18, Eq. 22 may then be rewritten as

$$\delta L_{\text{ine}} = \int_L \delta \mathbf{u}_\tau^{\mathrm{T}} \mathbf{M}^{\tau s} \ddot{\mathbf{u}}_\zeta \mathrm{d}s \tag{23}$$

In a form similar to those of $\mathbf{K}^{\tau\zeta}$ and $\mathbf{\Pi}^{\tau\zeta}$, $\mathbf{M}^{\tau\zeta}$ also includes 3×3 fundamental nuclei, which state

$$\mathbf{M}^{\tau\zeta} = \begin{bmatrix} E^{\rho}_{\tau\zeta H} & 0 & 0 \\ 0 & E^{\rho}_{\tau\zeta H} & 0 \\ 0 & 0 & E^{\rho}_{\tau\zeta H} \end{bmatrix} \tag{24}$$

where the diagonal element reads:

$$E^{\rho}_{\tau\zeta H} = \int_\Omega \rho \bar{F}_\tau \bar{F}_\zeta H \mathrm{d}\Omega \tag{25}$$

As far as the harmonic motion is concerned, the solution can be assumed to the following manner

$$\mathbf{u}_\zeta(s,t) = \mathbf{U}_\zeta(s) e^{i\omega t} \tag{26}$$

where $\mathbf{U}_\zeta(s)$ is the amplitude of the unknown displacement vector; ω is the angular frequency and i is equal to $\sqrt{-1}$. Eq. 26 transforms Eq. 21 and Eq. 23 from the time domain to the frequency domain. Thus, the resulting governing differential equation and natural boundary condition are:

$$\begin{gathered}\left(\mathbf{K}^{\tau\zeta}-\omega^2\mathbf{M}^{\tau\zeta}\right)\mathbf{U}_\zeta=0\\ \left[\mathbf{\Pi}^{\tau\zeta}\mathbf{U}_\zeta\right]|_{s=0}^{s=L}=\mathbf{P}_\zeta\end{gathered} \tag{27}$$

where $\mathbf{P}_\zeta$ is the amplitude of the generalized force vector acting at both ends of the beam.

5 Strong-form differential quadrature-based solutions

The Differential Quadrature Method (DQM) has shown its superior convergence property over the classical Finite Element Method and has been applied to discretize the strong-form governing equation of the CUF model for static analysis of straight composite beams. The present paper considers its further extension to curved metallic and composite beams. Within the framework of DQM, $\mathbf{U}_\zeta(s_i)$ and their higher-order derivatives at a point s_i can be expressed as a weighted linear combination of arbitrary test functions:

$$\begin{aligned}&\mathbf{U}_\zeta(s_i)=L_j(s_i)\mathbf{U}_{\zeta j}; \qquad i=1,2,....,n; \quad j=1,2,....,n\\ &\frac{\partial\mathbf{U}_\zeta(s_i)}{\partial s}=A_{ij}^{(1)}\mathbf{U}_{\zeta j}; \qquad i=1,2,....,n; \quad j=1,2,....,n\end{aligned} \tag{28}$$

where $L_j(s_i)$ is the weighting coefficient of $\mathbf{U}_\zeta(s_i)$; $A_{ij}^{(1)}$ represents the weighting matrix for its first derivative. n is the number of sampling points. According to literature [50], the Chebyshev nodal distribution was demonstrated to be the best choice due to the numerical accuracy and stability and its coordinate can be computed via the formulation:

$$s_i=\frac{L}{2}[1-cos(\frac{i-1}{n-1}\pi)]; \qquad i=1,2,\cdots,n \tag{29}$$

Evaluation of the value of the weighting matrix plays a crucial role in the algorithm implementation. As suggested by Shu [51], the Lagrangian polynomial basis is chosen for $L_j(s_i)$ and its derivative for $A_{ij}^{(1)}$, leading to:

$$\begin{aligned}&L_j(s_i)=\prod_{k=1,k\neq j}^{n}\left(\frac{s_i-s_k}{s_j-s_k}\right); \qquad i=1,2,....,n; \quad j=1,2,....,n\\ &A_{ij}^{(1)}=\frac{\phi\left(s_i\right)}{\phi\left(s_j\right)\left(s_i-s_j\right)}; \qquad i=1,2,....,n; \quad j=1,2,....,n; \quad i\neq j\\ &A_{ii}^{(1)}=-\sum_{j=1,j\neq i}^{n}A_{ij}^{(1)}; \qquad i=1,2,....,n\end{aligned} \tag{30}$$

where:

$$\phi(s_j)=\prod_{k=1,k\neq j}^{n}\left(s_j-s_k\right); \qquad j=1,2,\cdots,n \tag{31}$$

Subsequently, the explicit expression of the approximation for the higher-order derivative can be obtained recur-

sively, which states:

$$
\begin{aligned}
A_{ij}^{(m)} &= m\left(A_{ii}^{(m-1)}A_{ij}^{(1)} - \frac{A_{ij}^{(m-1)}}{s_i - s_j}\right); \qquad i,j = 1,2,\cdots,n; \quad m = 1,2,\cdots,n-1; \quad i \neq j \\
A_{ii}^{(m)} &= -\sum_{j=1,j\neq i}^{n} A_{ij}^{(m)}; \qquad i = 1,2,\cdots,n
\end{aligned}
\tag{32}
$$

Notice that the classical FEM also uses the Lagrangian polynomial basis for the formation of the shape function. However, its first derivative can not be computed via Eq. 30 since the Gauss integration point to be employed does not coincide with the element node in general. As a result, derivatives of the higher-order shape function are difficult to obtain and the lower-order counterpart is usually utilized in the classical FEM, the accuracy of which can only be enhanced by increasing the number of mesh generation. On the contrary, derivatives calculated by the DQ rule make it feasible for the employment of higher-order basis functions to approximate system variables, leading to the exponential convergence of solutions. In this manner, by substituting the weighting matrix in Eq. 30 and Eq. 32 into Eq. 27, a linear system of the algebraic equations of motion is given by:

$$
\begin{aligned}
\left(\mathbf{K}^{\tau\zeta ij} - \omega^2\mathbf{M}^{\tau\zeta ij}\right)\mathbf{U}_{\zeta j} &= 0 \\
\left[\mathbf{\Pi}^{\tau\zeta ij}\mathbf{U}_{\zeta j}\right]|_{s=0}^{s=L} &= \mathbf{P}_{\zeta j}
\end{aligned}
\tag{33}
$$

where components of $\mathbf{K}^{\tau\zeta ij}$, $\mathbf{\Pi}^{\tau\zeta ij}$ and $\mathbf{M}^{\tau\zeta ij}$ are expressed in Appendix A.

The implementation of the matrix assembly can be ensured by expanding the fundamental nucleus over indexes τ, ζ, i, and j. Generally speaking, the nodal stiffness matrix for the DQM can be formulated initially. After that, the matrix assembly in the cross-sectional domain can be done in the light of the p-version of FEM. For details of the formulation of global matrices, readers can refer to the literature [45]. Once global matrices are obtained, the eigenvalue problem can be finally solved via the imposition of boundary conditions, including the natural boundary condition and the essential boundary condition, as presented in the literature[44].

6 Numerical results

In this section, the promising feasibility of the DQ framework for the CUF-IHLE model is demonstrated through four numerical cases. In the first case, the vibration characteristics of metallic beams with different boundary conditions are investigated, whereas the remaining cases focus on composite beams with various lamination schemes. Besides, this section unveils the convergence performance of the proposed methodology as well as its exactness by comparison against 3D ABAQUS solutions.

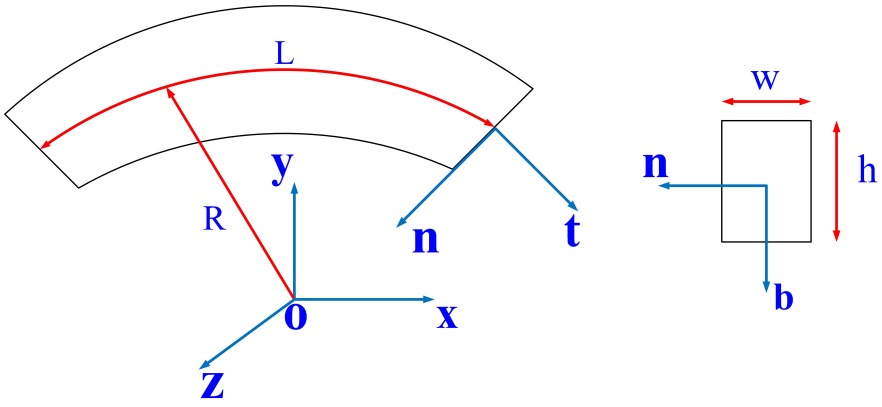

Figure 5: Geometrical shape of the metallic beam.

6.1 Metallic beam

The preliminary assessment considers a curved metallic beam with a square cross-section. The geometrical configuration is illustrated in Fig. 5. To be specific, the dimensions of the structure are given as: the width $b = 0.4$ m, the height $h = 0.6$ m, the length $L = \pi$ m and the radius $R = 2$ m. Accordingly, its material consists of an Aluminum alloy with the following isotropic properties: Young's modulus $E = 75$ Gpa, Poisson's ratio $\nu = 0.33$ and material density $\rho = 2700$ kg/m^3. Three classical, i.e., clamped (C), simply supported (S), and free (F) boundaries, are taken into account. In order to make a direct comparison between CUF-HLE and -IHLE models, the cross-sectional kinematics are defined in two separate sub-domains with two kinds of nodal numbering schemes, as depicted in Fig. 6.

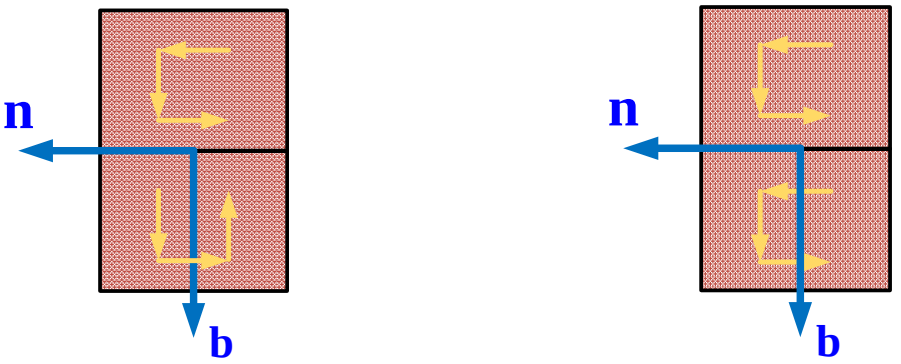

(a) Numbering scheme 1 (b) Numbering scheme 2

Figure 6: Metallic beam with different cross-sectional nodal numbering schemes.

Fig. 7 and 8 include the convergence curves of coupled bending/torsional and pure torsional modes with different boundary conditions, computed by CUF-HL3 and -IHL3 models, standing for the third polynomial degree. It can be seen that both frequency components obtained by the CUF-IHL3 model show perfect consistency, regardless of the alteration of nodal numbering schemes. However, the CUF-HL3 model spoiled such consistency, converging to different values as nodal numbering schemes vary. According to convergence analyses, The number of optimized collocation points (N) is 48 for the CF boundary condition and 40 for the CC boundary condition. Both of them are utilized to

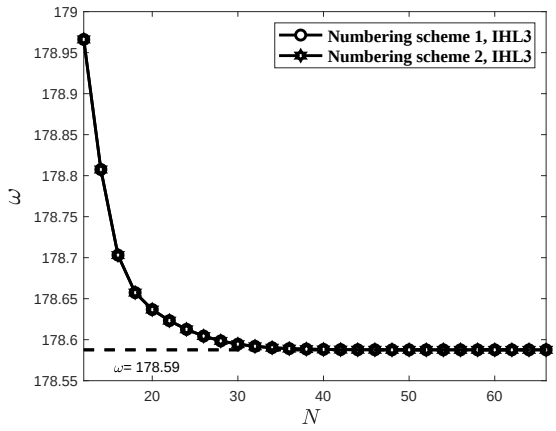

(a) Second bending/torsional (plane *xz*) frequency, IHL3

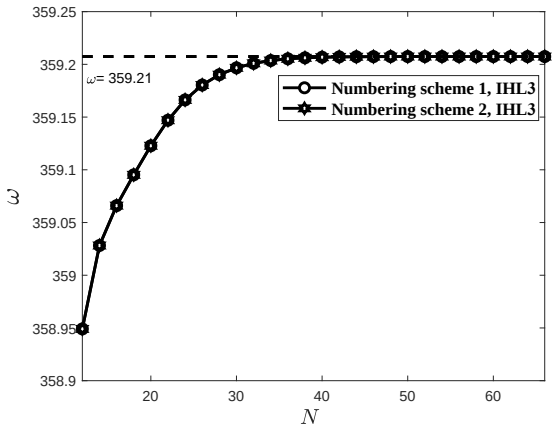

(b) First torsional frequency, IHL3

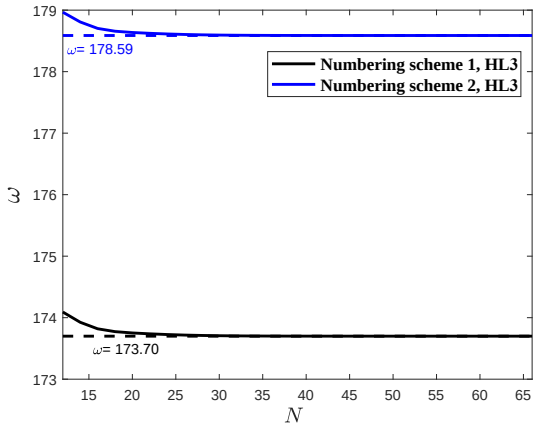

(c) Second bending/torsional (plane *xz*) frequency, HL3

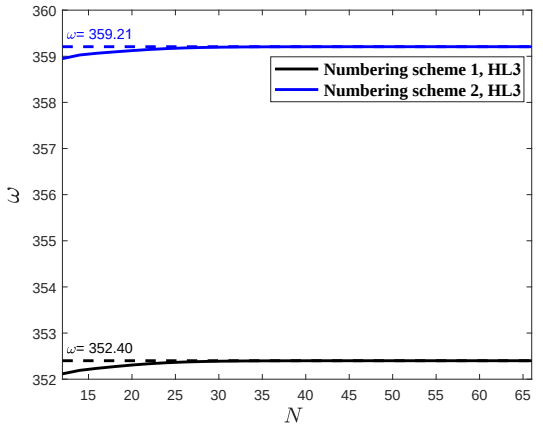

(d) First torsional frequency, HL3

Figure 7: Convergence of selected coupled and pure modes of the metallic beam by the two CUF-based models with different nodal numbering schemes (CF).

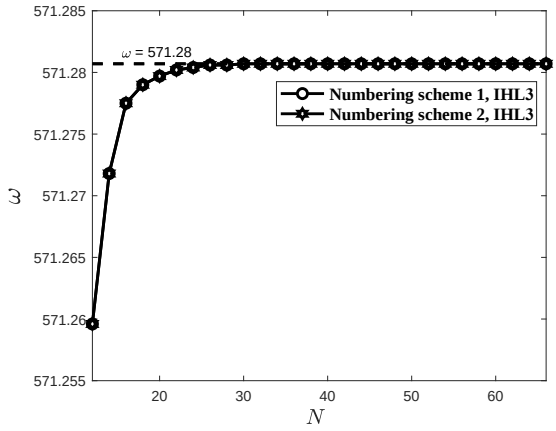

(a) First torsional frequency, IHL3

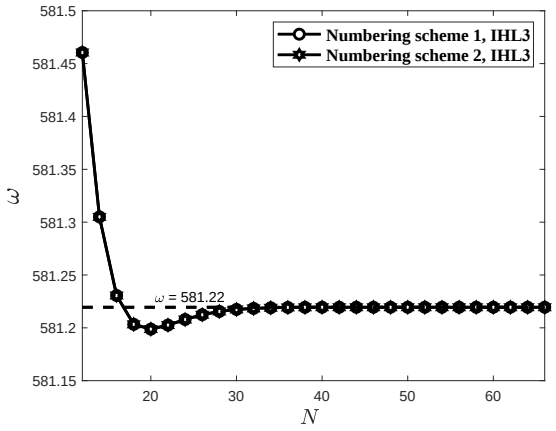

(b) Second bending/torsional (plane xz) frequency, IHL3

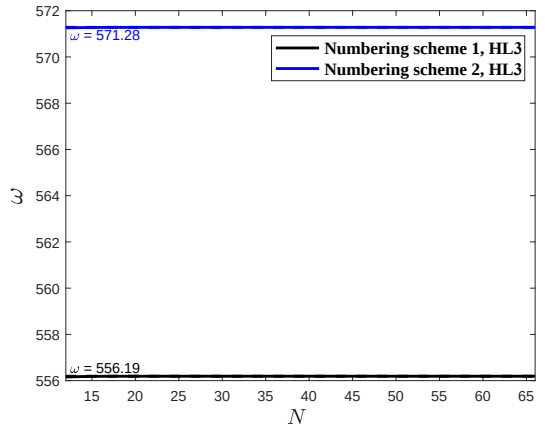

(c) First torsional frequency, HL3

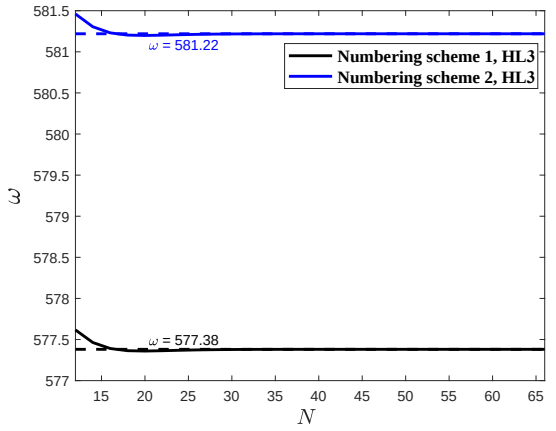

(d) Second bending/torsional (plane xz) frequency, HL3

Figure 8: Convergence of two coupled and pure modes of the metallic beam by the two CUF-based models with different nodal numbering schemes (CC).

evaluate the performance of the CUF-IHLE model with increasing kinematic orders.

Table 1: First five natural frequencies ω of the metallic beam for the CF boundary condition.

Model	mode 1[a]	mode 2[b]	mode 3[c]	mode 4[d]	mode 5[e]	DOFs
Abaqus-coarser 3D[f]	36.205	46.776	161.70	178.81	359.46	5595
Abaqus-finer 3D[g]	36.150	46.694	161.38	178.48	359.04	56463
Present CUF-IHLE solutions						
IHL3	36.160	46.740	161.50	178.59	359.21	2880
IHL4	36.140	46.703	161.34	178.49	359.07	4176
IHL5	36.134	46.683	161.30	178.41	358.96	5760

[a]: First flexural mode on plane xy

[b]: First flexural/torsional mode on plane xz

[c]: Second flexural mode on plane xy

[d]: Second flexural/torsional mode on plane xz

[e]: First torsional mode

[f]: Number of elements is $20 \times 4 \times 4$

[g]: Number of elements is $40 \times 10 \times 10$

Correspondingly, results ranging from mode 1 to 5 are listed in Table 1 and 2. 3D FEM solutions distinguished by the two Abaqus models with coarser and finer meshes are also incorporated for comparison purposes. It can be seen that results provided by the CUF-IHLE model are in high agreement with those by ABAQUS 3D models while maintaining significantly lower computational costs. In terms of reducing computational costs, the adoption of the CUF-IHL4 model can typically obtain the first five natural frequencies closer to ABAQUS-finer 3D solutions. Besides the exactness, the second bending/torsional mode on plane xz is apt to appear in mode 4 for the CF boundary condition. In contrast, mode 4 is characterized by the first torsional mode in the CC boundary condition. Such a mode switching phenomenon can be clearly seen in Fig. 9, which plots 3D deformations of mode 4 and 5 of the structure under these two different boundary conditions.

Table 2: First five natural frequencies ω of the metallic beam for the CC boundary condition.

Model	mode 1[a]	mode 2[b]	mode 3[c]	mode 4[d]	mode 5[e]	DOFs
Abaqus-coarser 3D[f]	249.04	390.70	446.20	571.24	582.77	5595
Abaqus-finer 3D[g]	248.23	390.41	444.66	570.50	580.98	56463
Present CUF-IHLE solutions						
IHL3	248.27	390.47	445.43	571.28	581.22	1800
IHL4	248.06	390.36	444.52	570.79	580.67	2610
IHL5	247.96	390.32	444.30	570.51	580.45	3600

[a]: First flexural/torsional mode on plane xz

[b]: First flexural mode on plane xy

[c]: Second flexural mode on plane xy

[d]: First torsional mode

[e]: Second flexural/torsional mode on plane xz

[f]: Number of elements is $20 \times 4 \times 4$

[g]: Number of elements is $40 \times 10 \times 10$

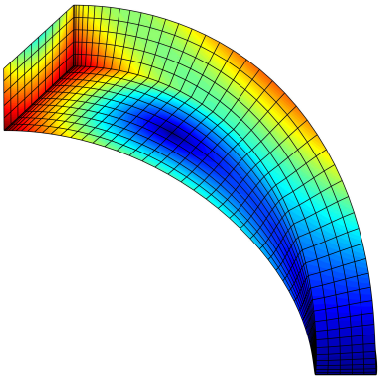

(a) Second bending/torsional (plane xz) mode, CF

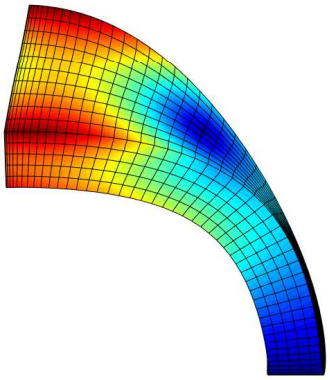

(b) First torsional mode, CF

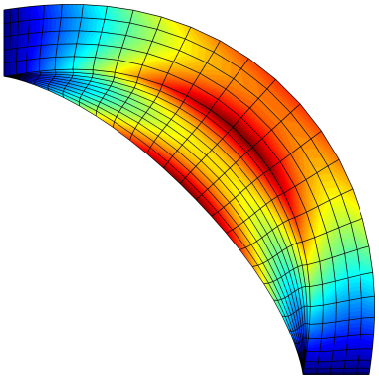

(c) First torsional mode, CC

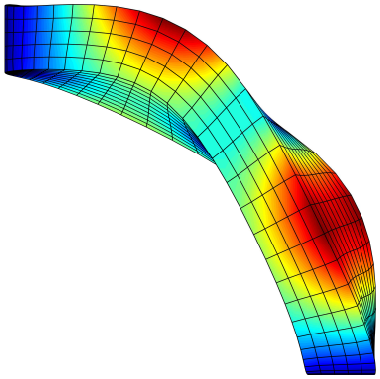

(d) Second bending/torsional (plane xz) mode, CC

Figure 9: 3D mode shapes of the fourth and fifth mode shapes for different boundary conditions.

6.2 Two-layer cross-ply laminated beam

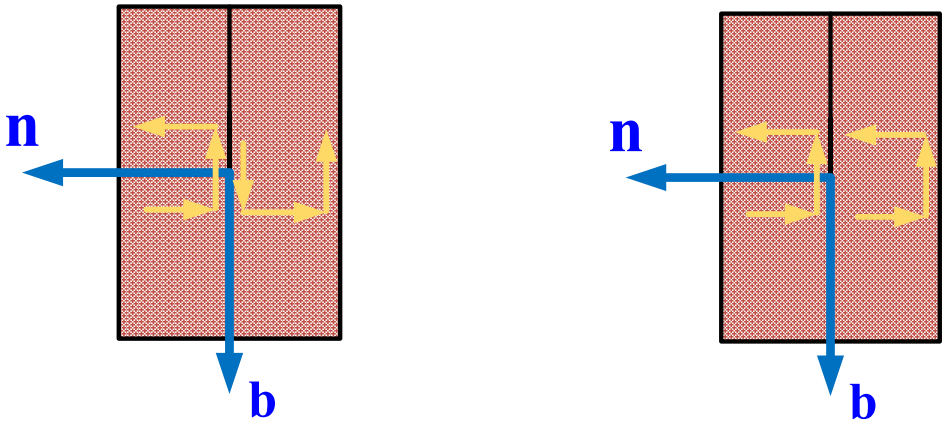

(a) Numbering scheme 1 (b) Numbering scheme 2

Figure 10: Cross-ply laminated beam with different cross-sectional nodal numbering schemes.

This section examines the performance of the proposed model in the cross-ply laminated beam. The structure is composed of two layers of the orthotropic material laminated together while keeping the same geometry (the length, width, and height) as in the previous case. Equal thickness is assumed for layers, the material properties of which are taken as $E_L = 250$ GPa, $E_T = 10$ GPa, $\nu_{LT} = 0.25$, $\nu_{TT} = 0.25$, $G_{LT} = 5$ GPa, $G_{TT} = 2$ GPa and $\rho = 2700$ kg/m^3, where subscripts L and T denote the direction parallel and perpendicular to the fibre, respectively. The stacking sequence is $[0^\circ/90^\circ]$, being the 90° fibre-oriented layer placed in the area of the positive **n** direction. To make a fair comparison of the two CUF-based models, we perform the discretization of the cross-section by different nodal numbering schemes, as shown in Fig. 10.

Fig. 11 represents the comparison of the coupled bending/torsional and pure torsional modes predicted by the two CUF models for a growing number of collocation points. It can be seen that CUF-IHLE solutions are not affected by the nodal numbering scheme at all. As a consequence of these results, accurate frequencies can be achieved with at least 30 collocation points, which are employed in the subsequent assessments of vibration characteristics of the curved cross-ply laminate.

Table 3 shows the corresponding numerical results of the first five natural frequencies obtained by CUF-IHLE and ABAQUS models. From the figure, we can see that the IHL3 model can predict more accurate flexural modes on plane xy compared to other modes benchmarked by the Abaqus-coarser 3D model. The IHLE model achieves desirable convergence for the polynomial order up to 8, whereas the Abaqus 3D tends to converge with degrees of freedom (DOFs) larger than 56463. The possible reason is that torsional modes characterized by intricate cross-sectional deformation patterns are not easily captured accurately unless more elements or higher-order kinematics are employed. A detailed 3D description of the first and fifth modes by CUF and ABAQUS models is given in Fig. 12, from which the cross-sectional warping in the torsional mode can be observed evidently.

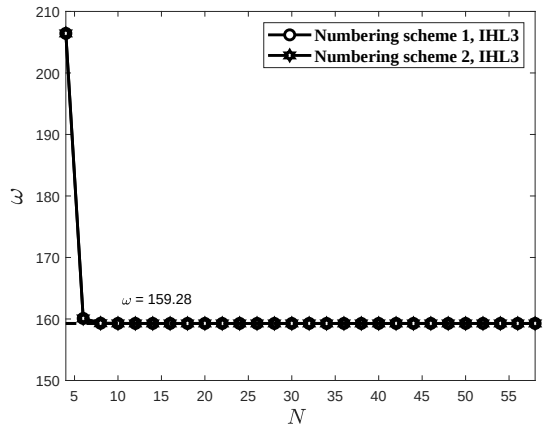

(a) First bending/torsional (plane xz) frequency, IHL3

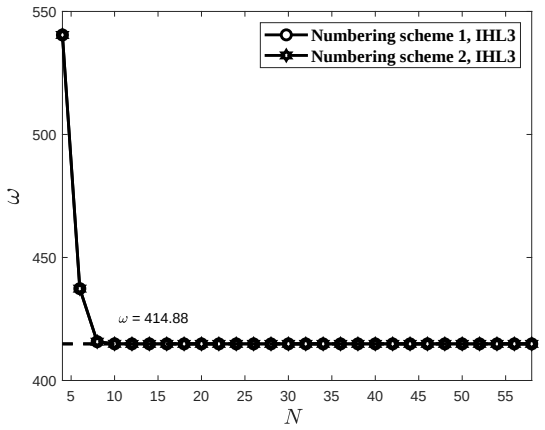

(b) First torsional frequency, IHL3

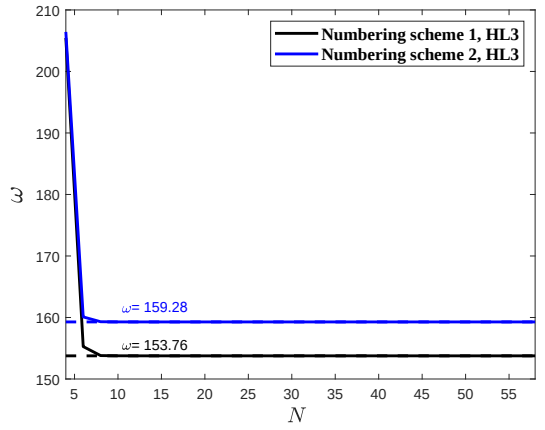

(c) First bending/torsional (plane xz) frequency, HL3

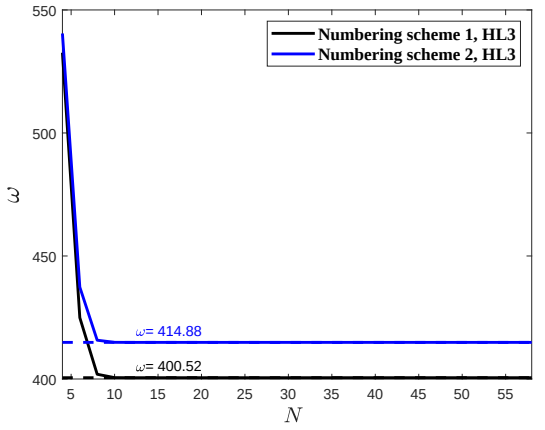

(d) First torsional frequency, HL3

Figure 11: Convergence of selected coupled and pure modes of the cross-ply laminate by the two CUF models with different nodal numbering schemes.

Table 3: First five natural frequencies ω of the cross-ply laminated beam.

Model	mode 1[a]	mode 2[b]	mode 3[c]	mode 4[d]	mode 5[e]	DOFs
Abaqus-coarser 3D[f]	159.04	245.99	287.91	367.65	413.15	5595
Abaqus-finer 3D[g]	158.70	245.10	287.52	366.54	413.33	56463
Present CUF-IHLE solutions						
IHL3	159.28	245.42	288.58	367.05	414.88	1800
IHL4	159.23	245.28	288.44	366.86	414.61	2610
IHL5	158.78	245.09	287.74	366.57	413.79	3600
IHL6	158.76	245.08	287.70	366.55	413.73	4770
IHL7	158.68	245.06	287.56	366.51	413.62	6120
IHL8	158.68	245.05	287.55	366.51	413.61	7650

[a]: First flexural/torsional mode on plane xz

[b]: First flexural mode on plane xy

[c]: Second flexural mode/torsional on plane xz

[d]: Second flexural mode on plane xy

[e]: First torsional mode

[f]: Number of elements is $20 \times 4 \times 4$

[g]: Number of elements is $40 \times 10 \times 10$

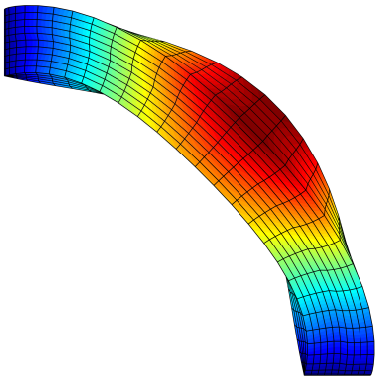

(a) First bending/torsional (plane *xz*) mode, IHL8

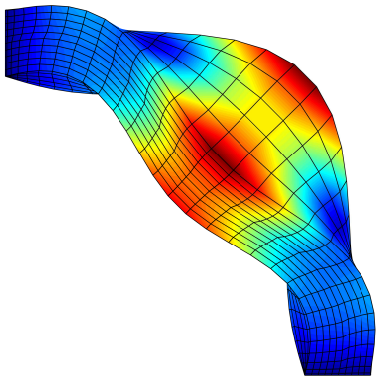

(b) First torsional mode, IHL8

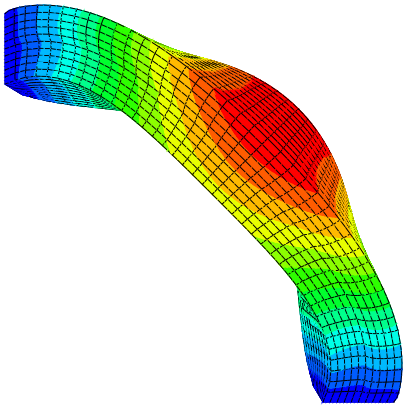

(c) First bending/torsional (plane *xz*) mode, ABAQUS

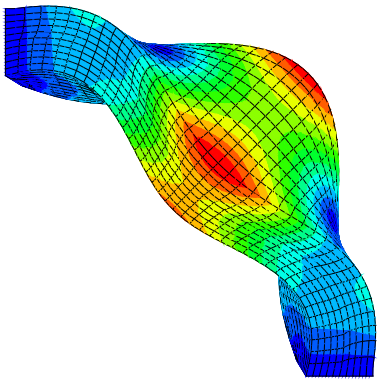

(d) First torsional mode, ABAQUS

Figure 12: Comparison of the first and fifth modes by CUF and ABAQUS.

6.3 Angle-ply laminated beam

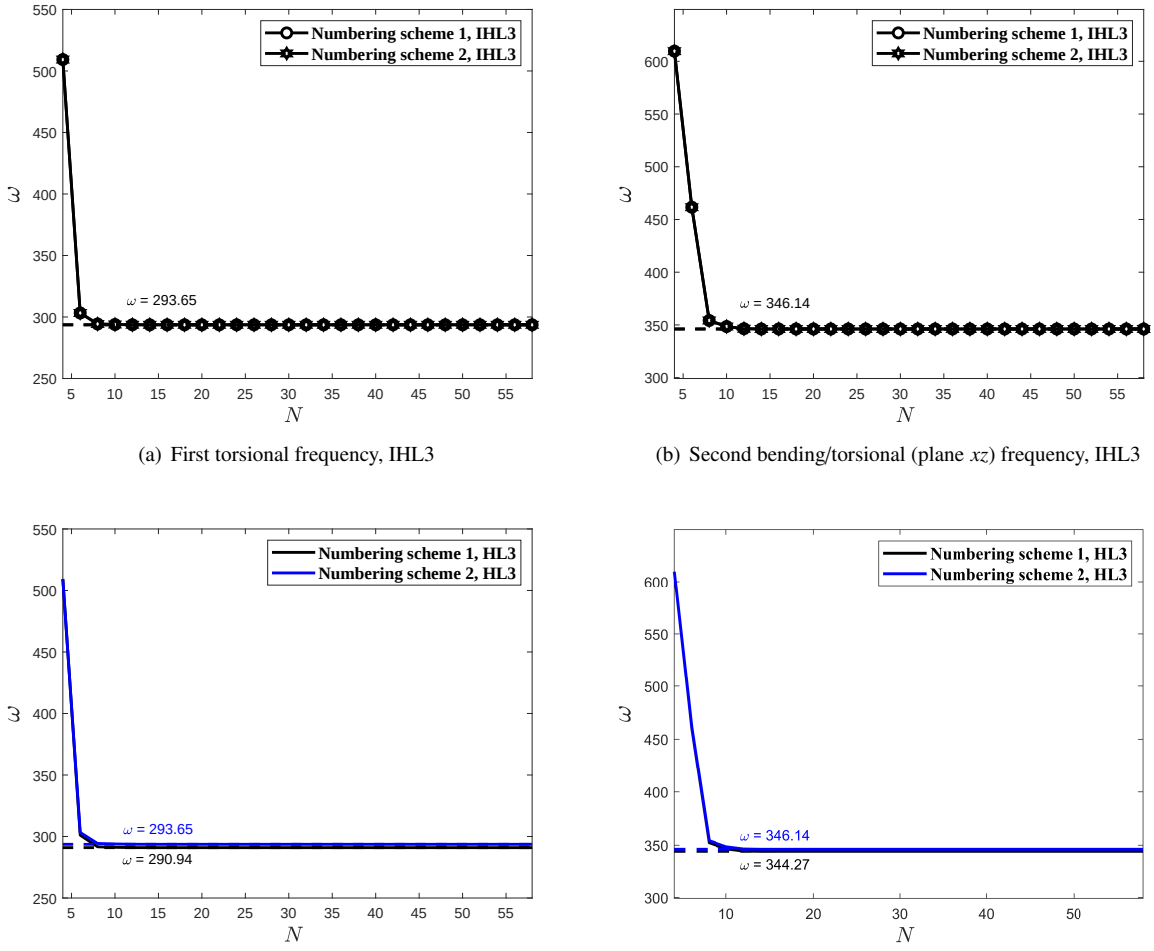

(a) First torsional frequency, IHL3

(b) Second bending/torsional (plane xz) frequency, IHL3

(c) First torsional frequency, HL3

(d) Second bending/torsional (plane xz) frequency, HL3

Figure 13: Convergence of two pure and coupled modes of the angle-ply laminate by the two CUF models with different nodal numbering schemes.

A further application to the angle-ply laminated beam is presented in this section. The same geometrical and material features as in the former case are selected again apart from the fibre orientation angle being $[-45^\circ/45^\circ]$ in the present case. Two types of cross-sectional nodal numbering schemes also remains unaltered. Fig.13 displays convergence curves of the two selected modes by the two CUF models with different nodal numbering schemes. It is seen from these plots that results obtained by CUF-IHL3 and -HL3 models indicate less discrepancy, although nodal numbering schemes are chosen in a different manner. The convergence is reached when the number of collocation points is 16, being an optimal candidate for the subsequent analysis. Table 4 gives detailed information about the first five natural frequencies. The number of DOFs is also provided for each model in the last column. It is noteworthy that the most challenging task is the computation of the bending/torsional (plane xz) and torsional modes, although IHLE solutions converge to ABAQUS-finer 3D as the order of the kinematics increases. Moreover, lower values can be achieved by IHL8 than ABAQUS-finer 3D models, while computational costs in terms of DOFs are also 14 times smaller. Two representative 3D modes calculated by CUF and ABAQUS models are shown in Fig. 14. The first torsional

Table 4: First five natural frequencies ω of the angle-ply laminated beam.

Model	mode 1[a]	mode 2[b]	mode 3[c]	mode 4[d]	mode 5[e]	DOFs
Abaqus-coarser 3D[f]	133.25	177.87	185.51	287.21	338.47	5595
Abaqus-finer 3D[g]	130.00	176.90	184.30	284.98	330.97	56463
Present CUF-IHLE solutions						
IHL3	136.58	178.38	185.77	293.65	346.14	960
IHL4	132.03	177.78	185.23	287.61	335.97	1392
IHL5	130.77	177.24	184.54	286.54	332.98	1920
IHL6	130.04	176.97	184.31	285.37	331.25	2544
IHL7	129.75	176.86	184.19	285.05	330.63	3264
IHL8	129.66	176.82	184.16	284.89	330.36	4080

[a]: First flexural/torsional mode on plane xz

[b]: First flexural mode on plane xy

[c]: Second flexural mode on plane xy

[d]: First torsional mode

[e]: Second flexural/torsional mode on plane xz

[f]: Number of elements is $20 \times 4 \times 4$

[g]: Number of elements is $40 \times 10 \times 10$

mode of the angle-ply laminate suffers less severe cross-sectional deformation than that of the cross-ply laminate, which may potentially account for the negligible difference between the numerical results of CUF models with distinct nodal numbering schemes in Fig. 13.

6.4 Sandwich beam

Table 5: Material properties of constituents in the sandwich structure

	Core	skin
E_1 (Gpa)	0.5776	276
E_2 (Gpa)	0.5776	6.9
E_3 (Gpa)	0.5776	6.9
G_{12} (Gpa)	0.1079	6.9
G_{13} (Gpa)	0.1079	6.9
G_{23} (Gpa)	0.22215	6.9
ν_{12}	0.0025	0.25
ν_{13}	0.0025	0.25
ν_{23}	0.0025	0.3
ρ (kg/m^3)	1000	681.8

The last assessment focuses on a sandwich beam, which is made of two Aluminum skins of 0.05 m thick each, and a soft core of 0.3 m. Other geometrical sizes and boundary conditions are the same as those of the cross-ply laminates. Material properties of the skin and core are listed in Table 5. The cross-sectional kinematics are composed of three sub-domains and described by two different nodal numbering schemes, as shown in Fig. 15.

Fig. 16 shows the convergence behavior of the two CUF models in terms of the second bending/torsional (plane xz) and the first torsional modes. As we can see that the convergence value of the second bending/torsional (plane xz) mode

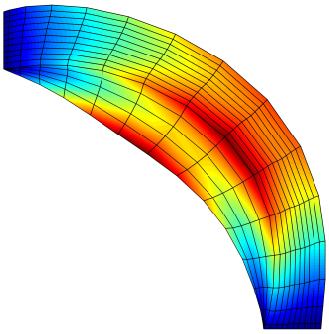

(a) First torsional mode, IHL8

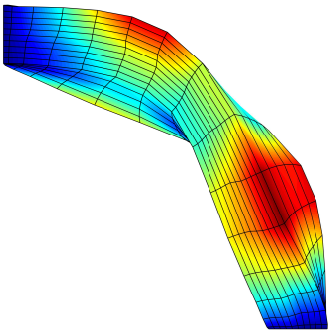

(b) Second bending/torsional (plane xz) mode, IHL8

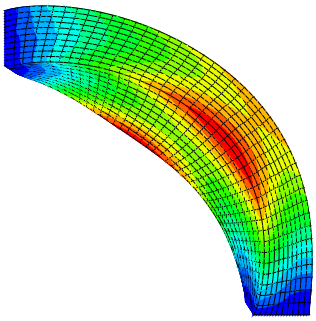

(c) First torsional mode, ABAQUS

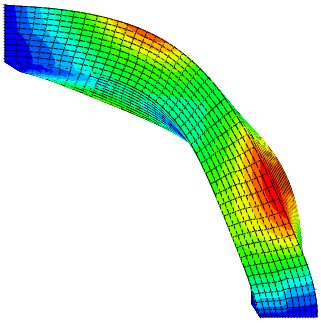

(d) Second bending/torsional (plane xz) mode, ABAQUS

Figure 14: Comparison of the fourth and fifth modes by CUF and ABAQUS.

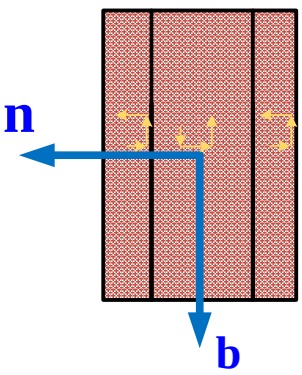

(a) Numbering scheme 1

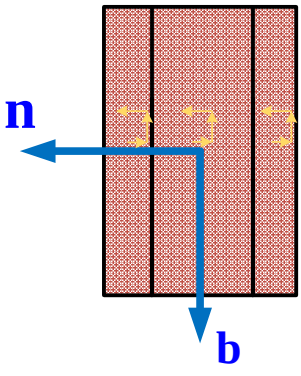

(b) Numbering scheme 2

Figure 15: Sandwich beam with different cross-sectional nodal numbering schemes.

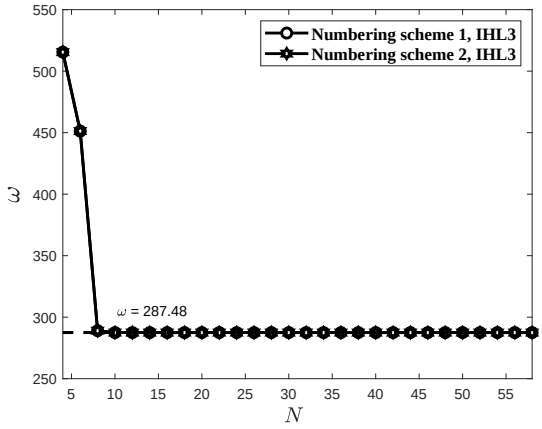

(a) Second bending/torsional (plane xz) frequency, IHL3

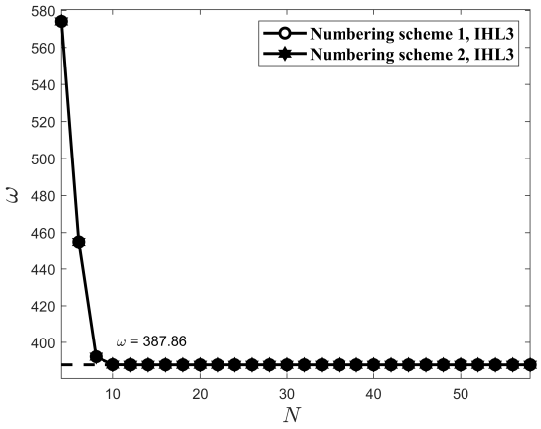

(b) First torsional frequency, IHL3

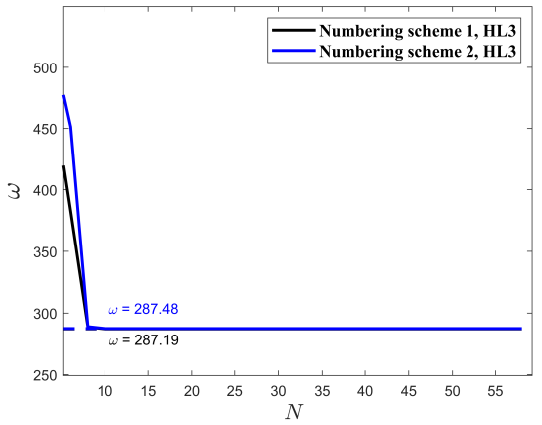

(c) Second bending/torsional (plane xz) frequency, HL3

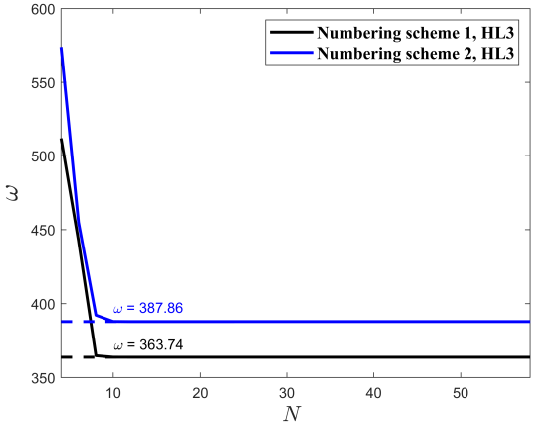

(d) First torsional frequency, HL3

Figure 16: Convergence of coupled and pure modes of the sandwich beam by the two CUF models with different nodal numbering schemes.

is less affected by variations of the nodal numbering scheme for both CUF models. Regarding the prediction of the first torsional mode, CUF-IHL3 solutions show a better convergence property than CUF-HL3. This phenomenon proves the validity of the CUF model based on IHLE kinematics as compared to prevailing HLE kinematics. 26 collocation points will be chosen in the following investigation to illustrate its superior behavior further.

Table 6: First five natural frequencies ω of the sandwich beam.

Model	mode 1[a]	mode 2[b]	mode 3[c]	mode 4[d]	mode 5[e]	DOFs
Abaqus-coarser 3D[f]	148.25	168.28	247.97	286.19	386.33	5595
Abaqus-finer 3D[g]	147.31	167.55	245.70	285.08	384.76	56463
Present CUF-IHLE solutions						
IHL3	147.30	168.37	245.59	287.48	387.86	2184
IHL4	147.29	168.31	245.58	287.39	387.72	3198
IHL5	147.28	167.62	245.55	285.58	385.52	4446
IHL6	147.28	167.57	245.55	285.38	385.28	5928
IHL7	147.28	167.47	245.54	285.16	384.94	7644
IHL8	147.28	167.45	245.54	285.08	384.84	9594

[a]: First flexural mode on plane *xy*

[b]: First flexural/torsional mode on plane *xz*

[c]: Second flexural mode on plane *xy*

[d]: Second flexural/torsional mode on plane *xz*

[e]: First torsional mode

[f]: Number of elements is $20 \times 4 \times 4$

[g]: Number of elements is $40 \times 10 \times 10$

Table 6 includes the effect of the polynomial order of the IHLE on the first five natural frequencies and the results of the ABAQUS model. It is possible to observe that the determination of bending/torsional (plane *xz*) and torsional modes can be remarkably demanding due to the high transverse anisotropy of the materials. At least a fifth-order model (IHL5) is required to obtain more accurate values of these modes as compared with those by the ABAQUS-coarser 3D model. Nonetheless, the number of DOFs of the IHL5 model is still lower than that of the ABAQUS-coarser 3D. Finally, as the polynomial order increases until the 8^{th}, the first three modes reach the convergence, better than the ABAQUS-finer 3D model. Regarding the high-fidelity solutions of mode 4 and 5, More DOFs, i.e., higher polynomial orders, are needed, being computation costs still in the acceptable range.

A 3D plot of the modes as mentioned above is given in Fig.17, from which we can clearly see the coupling of in-plane and out-of-plane deformations appearing in mode 4 and 5. Such complicated profiles are responsible for increasing computational efforts in the CUF-IHLE model.

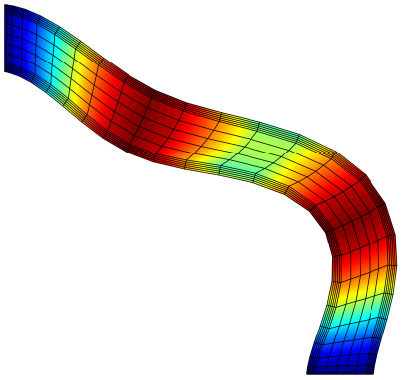

(a) First bending (plane xy) mode

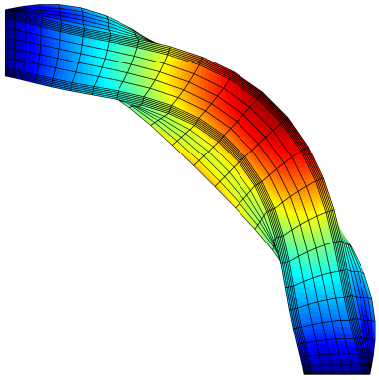

(b) First bending/torsional (plane xz) mode

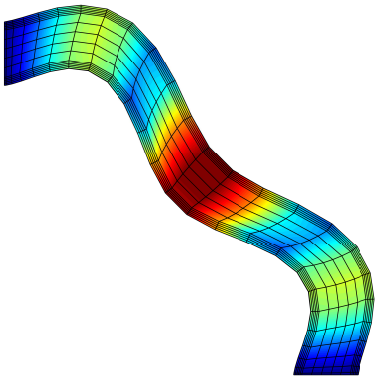

(c) Second bending (plane xy) mode

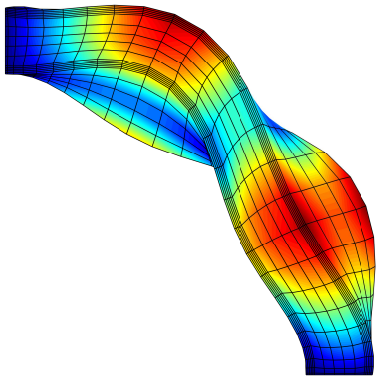

(d) Second bending/torsional (plane xz) mode

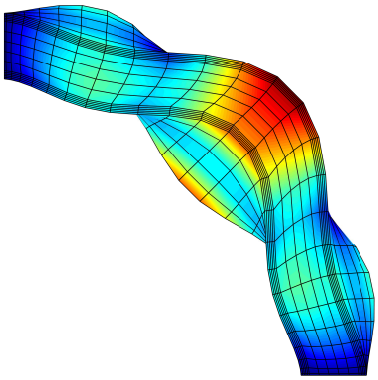

(e) First torsional mode

Figure 17: First five modes for the sandwich beam via IHL8.

7 Conclusions

Based on the Carrera Unified Formulation, the present paper aims to introduce an improved hierarchical Legendre-type beam model, and DQM has been subsequently applied to solve the differential equation of motion. Many examples have been carried out to demonstrate its power for free vibration analyses of curved metallic and laminated beams subjected to various boundary conditions. Among the results, the main finding can be summarized as follows:

1. Natural frequencies provided by the CUF-IHLE model are not affected by the nodal numbering scheme for all cases, although in terms of the CUF-HLE model, this influence becomes evident for most cases.

2. By virtue of the exponential convergence of DQM and the Layer-Wise property of the CUF-IHLE model, accurate frequency values can be obtained with greater efficiency than those offered by 3D ABAQUS results.

3. Lower-order models can not capture the vibration mode accompanied by the complex cross-sectional deformation. Higher-order models are strongly recommended, still with less computational costs compared to 3D ABAQUS results. Besides, the alteration of boundary conditions will change the order in which higher-order modes appear.

Although DQM-based solutions of the higher-order CUF beam model lead to improved accuracy over FEM solutions, the stiffness matrix produced by this method is non-positive definite. The future work focuses on the use of the alternative method to DQM, such as the quadrature element method (QEM), which integrates the efficient numerical integration scheme and the differential quadrature rule for the derivative approximation in a variational method. Such the method yields a positive definite matrix while maintaining the global approximation of 1D generalized displacements with high-order basis functions. [52, 53].

Acknowledgments

The first author would like to acknowledge the support by the National Natural Science Foundation of China (Grant No. 12002012).

Appendix A Fundamental nuclei

A.1 Expressions for $\mathbf{K}^{\tau\zeta}$ and $\mathbf{\Pi}^{\tau\zeta}$

$$
\begin{aligned}
K_{11}^{\tau\zeta} =& E_{\tau,\eta\zeta,\eta H}^{44} - E_{\tau\zeta\frac{1}{H}}^{22}\frac{\partial^2}{\partial s^2} + E_{\tau,\xi\zeta,\xi H}^{66} + \kappa(E_{\tau\zeta,\xi}^{66} + E_{\tau,\xi\zeta}^{66}) + \kappa^2 E_{\tau s\frac{1}{H}}^{66} \\
& - E_{\tau\zeta,\xi}^{26}\frac{\partial}{\partial s} + E_{\tau,\xi\zeta}^{26}\frac{\partial}{\partial s} + E_{\tau,\xi\zeta,\eta H}^{46} + E_{\tau,\eta\zeta,\xi H}^{46} + \kappa(E_{\tau\zeta,\eta}^{46} + E_{\tau,\eta\zeta}^{46}) \\
& - E_{\tau\zeta,\eta}^{24}\frac{\partial}{\partial s} + E_{\tau,\eta\zeta}^{24}\frac{\partial}{\partial s} \\
K_{12}^{\tau\zeta} =& \left[-E_{\tau\zeta,\xi}^{23} + E_{\tau,\xi\zeta}^{66} + \kappa(E_{\tau\zeta\frac{1}{H}}^{66} + E_{\tau\zeta\frac{1}{H}}^{22})\right]\frac{\partial}{\partial s} + E_{\tau,\eta\zeta,\eta H}^{45} + E_{\tau,\xi\zeta,\xi H}^{36} \\
& + \kappa E_{\tau\zeta,\xi}^{36} - \kappa E_{\tau,\xi\zeta}^{26} - \kappa^2 E_{\tau\zeta\frac{1}{H}}^{26} - E_{\tau\zeta\frac{1}{H}}^{26}\frac{\partial^2}{\partial s^2} + E_{\tau,\eta\zeta,\xi H}^{34} - \kappa E_{\tau,\eta\zeta}^{24} \\
& - E_{\tau\zeta,\eta}^{25}\frac{\partial}{\partial s} + E_{\tau,\xi\zeta,\eta H}^{56} + \kappa E_{\tau\zeta,\eta}^{56} + E_{\tau,\eta\zeta}^{46}\frac{\partial}{\partial s} \\
K_{13}^{\tau\zeta} =& \left(-E_{\tau\zeta,\eta}^{12} + E_{\tau,\eta\zeta}^{44}\right)\frac{\partial}{\partial s} + E_{\tau,\eta\zeta,\xi H}^{45} + E_{\tau,\xi\zeta,\eta H}^{16} + \kappa E_{\tau\zeta,\eta}^{16} + E_{\tau,\eta\zeta,\eta H}^{14} \\
& - E_{\tau\zeta,\xi}^{25}\frac{\partial}{\partial s} + E_{\tau,\xi\zeta,\xi H}^{56} + \kappa E_{\tau\zeta,\xi}^{56} + (E_{\tau,\xi\zeta}^{46} + \kappa E_{\tau\zeta\frac{1}{H}}^{46})\frac{\partial}{\partial s} - E_{\tau\zeta\frac{1}{H}}^{24}\frac{\partial^2}{\partial s^2} \\
K_{21}^{\tau\zeta} =& \left[E_{\tau,\xi\zeta}^{23} - E_{\tau\zeta,\xi}^{66} - \kappa(E_{\tau\zeta\frac{1}{H}}^{66} + E_{\tau s\frac{1}{H}}^{22})\right]\frac{\partial}{\partial s} + E_{\tau,\eta\zeta,\eta H}^{45} + E_{\tau,\xi\zeta,\xi H}^{36} \\
& + \kappa E_{\tau,\xi\zeta}^{36} - \kappa E_{\tau\zeta,\xi}^{26} - \kappa^2 E_{\tau\zeta\frac{1}{H}}^{26} - E_{\tau\zeta\frac{1}{H}}^{26}\frac{\partial^2}{\partial s^2} + E_{\tau,\xi\zeta,\eta H}^{34} - \kappa E_{\tau\zeta,\eta}^{24} \\
& - E_{\tau\zeta,\eta}^{46}\frac{\partial}{\partial s} + E_{\tau,\eta\zeta,\xi H}^{56} + \kappa E_{\tau,\eta\zeta}^{56} + E_{\tau,\eta\zeta}^{25}\frac{\partial}{\partial s} \\
K_{22}^{\tau\zeta} =& E_{\tau,\xi\zeta,\xi H}^{33} + E_{\tau,\eta\zeta,\eta H}^{55} - E_{\tau\zeta\frac{1}{H}}^{66}\frac{\partial^2}{\partial s^2} - \kappa(E_{\tau,\xi\zeta}^{23} + E_{\tau\zeta,\xi}^{23}) + \kappa^2 E_{\tau\zeta\frac{1}{H}}^{22} \\
& - E_{\tau\zeta,\xi}^{36}\frac{\partial}{\partial s} + E_{\tau,\xi\zeta}^{36}\frac{\partial}{\partial s} + E_{\tau,\xi\zeta,\eta H}^{35} + E_{\tau,\eta\zeta,\xi H}^{35} - \kappa E_{\tau\zeta,\eta}^{25} - \kappa E_{\tau,\eta\zeta}^{25} \\
& - E_{\tau\zeta,\eta}^{56}\frac{\partial}{\partial s} + E_{\tau,\eta\zeta}^{56}\frac{\partial}{\partial s} \\
K_{23}^{\tau\zeta} =& E_{\tau,\xi\zeta,\eta H}^{13} + E_{\tau,\eta\zeta,\xi H}^{55} - \kappa E_{\tau\zeta,\eta}^{12} - E_{\tau\zeta,\eta}^{16}\frac{\partial}{\partial s} + E_{\tau,\eta\zeta}^{45}\frac{\partial}{\partial s} + E_{\tau,\xi\zeta,\xi H}^{35} \\
& + E_{\tau,\eta\zeta,\eta H}^{15} - \kappa E_{\tau\zeta,\xi}^{25} - E_{\tau\zeta,\xi}^{56}\frac{\partial}{\partial s} + E_{\tau,\xi\zeta}^{34}\frac{\partial}{\partial s} - \kappa E_{\tau\zeta\frac{1}{H}}^{24}\frac{\partial}{\partial s} - E_{\tau\zeta\frac{1}{H}}^{46}\frac{\partial^2}{\partial s^2} \\
K_{31}^{\tau\zeta} =& \left(E_{\tau,\eta\zeta}^{12} - E_{\tau\zeta,\eta}^{44}\right)\frac{\partial}{\partial s} + E_{\tau,\xi\zeta,\eta H}^{45} + E_{\tau,\eta\zeta,\xi H}^{16} + \kappa E_{\tau,\eta\zeta}^{16} + E_{\tau,\eta\zeta,\eta H}^{14} \\
& + E_{\tau,\xi\zeta,\xi H}^{56} + \kappa E_{\tau,\xi\zeta}^{56} - E_{\tau\zeta,\xi}^{46}\frac{\partial}{\partial s} - \kappa E_{\tau\zeta\frac{1}{H}}^{46}\frac{\partial}{\partial s} + E_{\tau,\xi\zeta}^{25}\frac{\partial}{\partial s} - E_{\tau\zeta\frac{1}{H}}^{24}\frac{\partial^2}{\partial s^2} \\
K_{32}^{\tau\zeta} =& E_{\tau,\eta\zeta,\xi H}^{13} + E_{\tau,\xi\zeta,\eta H}^{55} - \kappa E_{\tau,\eta\zeta}^{12} - E_{\tau\zeta,\eta}^{45}\frac{\partial}{\partial s} + E_{\tau,\eta\zeta}^{16}\frac{\partial}{\partial s} + E_{\tau,\xi\zeta,\xi H}^{35} \\
& + E_{\tau,\eta\zeta,\eta H}^{15} - \kappa E_{\tau,\xi\zeta}^{25} - E_{\tau\zeta,\xi}^{34}\frac{\partial}{\partial s} + \kappa E_{\tau\zeta\frac{1}{H}}^{24}\frac{\partial}{\partial s} + E_{\tau,\xi\zeta}^{56}\frac{\partial}{\partial s} - E_{\tau\zeta\frac{1}{H}}^{46}\frac{\partial^2}{\partial s^2} \\
K_{33}^{\tau\zeta} =& E_{\tau,\eta\zeta,\eta H}^{11} + E_{\tau,\xi\zeta,\xi H}^{55} - E_{\tau s\frac{1}{H}}^{44}\frac{\partial^2}{\partial s^2} - E_{\tau\zeta,\xi}^{45}\frac{\partial}{\partial s} + E_{\tau,\xi\zeta}^{45}\frac{\partial}{\partial s} + E_{\tau,\xi\zeta,\eta H}^{15} \\
& + E_{\tau,\eta\zeta,\xi H}^{15} - E_{\tau\zeta,\eta}^{14}\frac{\partial}{\partial s} + E_{\tau,\eta\zeta}^{14}\frac{\partial}{\partial s}
\end{aligned}
\tag{A.1}
$$

where general algebraic terms $E^{\alpha\beta}_{\tau_{,\xi}\zeta_{,\eta}}$, $E^{\alpha\beta}_{\tau_{,\xi}\zeta_{,\eta}H}$ and $E^{\alpha\beta}_{\tau_{,\xi}\zeta_{,\eta}\frac{1}{H}}$ are integrals over the cross-section:

$$\begin{aligned}
E^{\alpha\beta}_{\tau_{,\xi}\zeta_{,\eta}} &= \int_\Omega \tilde{C}_{\alpha\beta}\bar{F}_{\tau_{,\xi}}\bar{F}_{\zeta,\eta}\mathrm{d}\Omega \\
E^{\alpha\beta}_{\tau_{,\xi}\zeta_{,\eta}H} &= \int_\Omega \tilde{C}_{\alpha\beta}\bar{F}_{\tau_{,\xi}}\bar{F}_{\zeta,\eta}H\mathrm{d}\Omega \\
E^{\alpha\beta}_{\tau_{,\xi}\zeta_{,\eta}\frac{1}{H}} &= \int_\Omega \tilde{C}_{\alpha\beta}\bar{F}_{\tau_{,\xi}}\bar{F}_{\zeta,\eta}\frac{1}{H}\mathrm{d}\Omega
\end{aligned} \tag{A.2}$$

where the suffix after the comma indicates the derivative. As concerns about natural boundary conditions, components of $\mathbf{\Pi}^{\tau\zeta}$ have the expression

$$\begin{aligned}
&\Pi^{\tau\zeta}_{11} = E^{22}_{\tau\zeta\frac{1}{H}}\frac{\partial}{\partial s}+E^{26}_{\tau\zeta,\xi}+\kappa E^{26}_{\tau\zeta\frac{1}{H}}+E^{24}_{\tau\zeta,\eta}, && \Pi^{\tau\zeta}_{12} = E^{23}_{\tau\zeta,\xi}-\kappa E^{22}_{\tau\zeta\frac{1}{H}}+E^{26}_{\tau\zeta\frac{1}{H}}\frac{\partial}{\partial s}+E^{25}_{\tau\zeta,\eta}, && \Pi^{\tau\zeta}_{13} = E^{12}_{\tau\zeta,\eta}+E^{25}_{\tau\zeta,\xi}+E^{24}_{\tau\zeta\frac{1}{H}}\frac{\partial}{\partial s} \\
&\Pi^{\tau\zeta}_{21} = E^{66}_{\tau\zeta,\xi}+\kappa E^{66}_{\tau s\frac{1}{H}}+E^{26}_{\tau\zeta\frac{1}{H}}\frac{\partial}{\partial s}+E^{46}_{\tau\zeta,\eta}, && \Pi^{\tau\zeta}_{22} = E^{66}_{\tau\zeta\frac{1}{H}}\frac{\partial}{\partial s}+E^{36}_{\tau\zeta,\xi}-\kappa E^{26}_{\tau\zeta\frac{1}{H}}+E^{56}_{\tau\zeta,\eta}, && \Pi^{\tau\zeta}_{23} = E^{16}_{\tau\zeta,\eta}+E^{56}_{\tau\zeta,\xi}+E^{46}_{\tau\zeta\frac{1}{H}} \\
&\Pi^{\tau\zeta}_{31} = E^{44}_{\tau\zeta,\eta}+E^{46}_{\tau\zeta,\xi}+\kappa E^{46}_{\tau s\frac{1}{H}}+E^{24}_{\tau\zeta\frac{1}{H}}\frac{\partial}{\partial s}, && \Pi^{\tau\zeta}_{32} = E^{45}_{\tau\zeta,\eta}+E^{34}_{\tau\zeta,\xi}-\kappa E^{24}_{\tau\zeta\frac{1}{H}}+E^{46}_{\tau\zeta\frac{1}{H}}\frac{\partial}{\partial s}, && \Pi^{\tau\zeta}_{33} = E^{44}_{\tau s\frac{1}{H}}\frac{\partial}{\partial s}+E^{45}_{\tau\zeta,\xi}+E^{14}_{\tau\zeta,\eta}
\end{aligned} \tag{A.3}$$

A.2 Expressions for $\mathbf{K}^{\tau\zeta ij}$, $\mathbf{\Pi}^{\tau\zeta ij}$ and $\mathbf{M}^{\tau\zeta ij}$

$$
\begin{aligned}
K_{11}^{\tau\zeta ij} =& E^{44}_{\tau,\eta\zeta,\eta H} L_j(s_i) - E^{22}_{\tau\zeta\,\frac{1}{H}} A^{(2)}_{ij} + E^{66}_{\tau,\xi\zeta,\xi H} L_j(s_i) + \kappa(E^{66}_{\tau\zeta,\xi} + E^{66}_{\tau,\xi\zeta}) L_j(s_i) + \kappa^2 E^{66}_{\tau s\,\frac{1}{H}} L_j(s_i) \\
& - E^{26}_{\tau\zeta,\xi} A^{(1)}_{ij} + E^{26}_{\tau,\xi\zeta} A^{(1)}_{ij} + E^{46}_{\tau,\xi\zeta,\eta H} L_j(s_i) + E^{46}_{\tau,\eta\zeta,\xi H} L_j(s_i) + \kappa(E^{46}_{\tau\zeta,\eta} + E^{46}_{\tau,\eta\zeta}) L_j(s_i) \\
& - E^{24}_{\tau\zeta,\eta} A^{(1)}_{ij} + E^{24}_{\tau,\eta\zeta} A^{(1)}_{ij} \\
K_{12}^{\tau\zeta ij} =& \left[-E^{23}_{\tau\zeta,\xi} + E^{66}_{\tau,\xi\zeta} + \kappa(E^{66}_{\tau\zeta\,\frac{1}{H}} + E^{22}_{\tau\zeta\,\frac{1}{H}}) \right] A^{(1)}_{ij} + E^{45}_{\tau,\eta\zeta,\eta H} L_j(s_i) + E^{36}_{\tau,\xi\zeta,\xi H} L_j(s_i) \\
& + \kappa E^{36}_{\tau\zeta,\xi} L_j(s_i) - \kappa E^{26}_{\tau,\xi\zeta} L_j(s_i) - \kappa^2 E^{26}_{\tau\zeta\,\frac{1}{H}} L_j(s_i) - E^{26}_{\tau\zeta\,\frac{1}{H}} A^{(2)}_{ij} + E^{34}_{\tau,\eta\zeta,\xi H} L_j(s_i) - \kappa E^{24}_{\tau,\eta\zeta} L_j(s_i) \\
& - E^{25}_{\tau\zeta,\eta} A^{(1)}_{ij} + E^{56}_{\tau,\xi\zeta,\eta H} L_j(s_i) + \kappa E^{56}_{\tau\zeta,\eta} L_j(s_i) + E^{46}_{\tau,\eta\zeta} A^{(1)}_{ij} \\
K_{13}^{\tau\zeta ij} =& \left(-E^{12}_{\tau\zeta,\eta} + E^{44}_{\tau,\eta\zeta} \right) A^{(1)}_{ij} + E^{45}_{\tau,\eta\zeta,\xi H} L_j(s_i) + E^{16}_{\tau,\xi\zeta,\eta H} L_j(s_i) + \kappa E^{16}_{\tau\zeta,\eta} L_j(s_i) + E^{14}_{\tau,\eta\zeta,\eta H} L_j(s_i) \\
& - E^{25}_{\tau\zeta,\xi} A^{(1)}_{ij} + E^{56}_{\tau,\xi\zeta,\xi H} L_j(s_i) + \kappa E^{56}_{\tau\zeta,\xi} L_j(s_i) + (E^{46}_{\tau,\xi\zeta} + \kappa E^{46}_{\tau\zeta\,\frac{1}{H}}) A^{(1)}_{ij} - E^{24}_{\tau\zeta\,\frac{1}{H}} A^{(2)}_{ij} \\
K_{21}^{\tau\zeta ij} =& \left[E^{23}_{\tau,\xi\zeta} - E^{66}_{\tau\zeta,\xi} - \kappa(E^{66}_{\tau\zeta\,\frac{1}{H}} + E^{22}_{\tau s\,\frac{1}{H}}) \right] A^{(1)}_{ij} + E^{45}_{\tau,\eta\zeta,\eta H} L_j(s_i) + E^{36}_{\tau,\xi\zeta,\xi H} L_j(s_i) \\
& + \kappa E^{36}_{\tau,\xi\zeta} L_j(s_i) - \kappa E^{26}_{\tau\zeta,\xi} L_j(s_i) - \kappa^2 E^{26}_{\tau\zeta\,\frac{1}{H}} L_j(s_i) - E^{26}_{\tau\zeta\,\frac{1}{H}} A^{(2)}_{ij} + E^{34}_{\tau,\xi\zeta,\eta H} L_j(s_i) - \kappa E^{24}_{\tau\zeta,\eta} L_j(s_i) \\
& - E^{46}_{\tau\zeta,\eta} A^{(1)}_{ij} + E^{56}_{\tau,\eta\zeta,\xi H} L_j(s_i) + \kappa E^{56}_{\tau,\eta\zeta} L_j(s_i) + E^{25}_{\tau,\eta\zeta} A^{(1)}_{ij} \\
K_{22}^{\tau\zeta ij} =& E^{33}_{\tau,\xi\zeta,\xi H} L_j(s_i) + E^{55}_{\tau,\eta\zeta,\eta H} L_j(s_i) - E^{66}_{\tau\zeta\,\frac{1}{H}} A^{(2)}_{ij} - \kappa(E^{23}_{\tau,\xi\zeta} + E^{23}_{\tau\zeta,\xi}) L_j(s_i) + \kappa^2 E^{22}_{\tau\zeta\,\frac{1}{H}} L_j(s_i) \\
& - E^{36}_{\tau\zeta,\xi} A^{(1)}_{ij} + E^{36}_{\tau,\xi\zeta} A^{(1)}_{ij} + E^{35}_{\tau,\xi\zeta,\eta H} L_j(s_i) + E^{35}_{\tau,\eta\zeta,\xi H} L_j(s_i) - \kappa E^{25}_{\tau\zeta,\eta} L_j(s_i) - \kappa E^{25}_{\tau,\eta\zeta} L_j(s_i) \\
& - E^{56}_{\tau\zeta,\eta} A^{(1)}_{ij} + E^{56}_{\tau,\eta\zeta} A^{(1)}_{ij} \\
K_{23}^{\tau\zeta ij} =& E^{13}_{\tau,\xi\zeta,\eta H} L_j(s_i) + E^{55}_{\tau,\eta\zeta,\xi H} L_j(s_i) - \kappa E^{12}_{\tau\zeta,\eta} L_j(s_i) - E^{16}_{\tau\zeta,\eta} A^{(1)}_{ij} + E^{45}_{\tau,\eta\zeta} A^{(1)}_{ij} + E^{35}_{\tau,\xi\zeta,\xi H} L_j(s_i) \\
& + E^{15}_{\tau,\eta\zeta,\eta H} L_j(s_i) - \kappa E^{25}_{\tau\zeta,\xi} L_j(s_i) - E^{56}_{\tau\zeta,\xi} A^{(1)}_{ij} + E^{34}_{\tau,\xi\zeta} A^{(1)}_{ij} - \kappa E^{24}_{\tau\zeta\,\frac{1}{H}} A^{(1)}_{ij} - E^{46}_{\tau\zeta\,\frac{1}{H}} A^{(2)}_{ij} \\
K_{31}^{\tau\zeta ij} =& \left(E^{12}_{\tau,\eta\zeta} - E^{44}_{\tau\zeta,\eta} \right) A^{(1)}_{ij} + E^{45}_{\tau,\xi\zeta,\eta H} L_j(s_i) + E^{16}_{\tau,\eta\zeta,\xi H} L_j(s_i) + \kappa E^{16}_{\tau,\eta\zeta} L_j(s_i) + E^{14}_{\tau,\eta\zeta,\eta H} L_j(s_i) \\
& + E^{56}_{\tau,\xi\zeta,\xi H} L_j(s_i) + \kappa E^{56}_{\tau,\xi\zeta} L_j(s_i) - E^{46}_{\tau\zeta,\xi} A^{(1)}_{ij} - \kappa E^{46}_{\tau\zeta\,\frac{1}{H}} A^{(1)}_{ij} + E^{25}_{\tau,\xi\zeta} A^{(1)}_{ij} - E^{24}_{\tau\zeta\,\frac{1}{H}} A^{(2)}_{ij} \\
K_{32}^{\tau\zeta ij} =& E^{13}_{\tau,\eta\zeta,\xi H} L_j(s_i) + E^{55}_{\tau,\eta\zeta,\eta H} L_j(s_i) - \kappa E^{12}_{\tau,\eta\zeta} L_j(s_i) - E^{45}_{\tau\zeta,\eta} A^{(1)}_{ij} + E^{16}_{\tau,\eta\zeta} A^{(1)}_{ij} + E^{35}_{\tau,\xi\zeta,\xi H} L_j(s_i) \\
& + E^{15}_{\tau,\eta\zeta,\eta H} L_j(s_i) - \kappa E^{25}_{\tau,\xi\zeta} L_j(s_i) - E^{34}_{\tau\zeta,\xi} A^{(1)}_{ij} + \kappa E^{24}_{\tau\zeta\,\frac{1}{H}} A^{(1)}_{ij} + E^{56}_{\tau,\xi\zeta} A^{(1)}_{ij} - E^{46}_{\tau\zeta\,\frac{1}{H}} A^{(2)}_{ij} \\
K_{33}^{\tau\zeta ij} =& E^{11}_{\tau,\eta\zeta,\eta H} L_j(s_i) + E^{55}_{\tau,\xi\zeta,\xi H} L_j(s_i) - E^{44}_{\tau s\,\frac{1}{H}} A^{(2)}_{ij} - E^{45}_{\tau\zeta,\xi} A^{(1)}_{ij} + E^{45}_{\tau,\xi\zeta} A^{(1)}_{ij} + E^{15}_{\tau,\xi\zeta,\eta H} L_j(s_i) \\
& + E^{15}_{\tau,\eta\zeta,\xi H} L_j(s_i) - E^{14}_{\tau\zeta,\eta} A^{(1)}_{ij} + E^{14}_{\tau,\eta\zeta} A^{(1)}_{ij}
\end{aligned}
\tag{A.4}
$$

$$
\begin{aligned}
\Pi_{11}^{\tau\zeta ij} =& E^{22}_{\tau\zeta_{\frac{1}{H}}} A^{(1)}_{ij} + E^{26}_{\tau\zeta_{,\xi}} L_j(s_i) + \kappa E^{26}_{\tau\zeta_{\frac{1}{H}}} L_j(s_i) + E^{24}_{\tau\zeta_{,\eta}} L_j(s_i) \\
\Pi_{12}^{\tau\zeta ij} =& E^{23}_{\tau\zeta_{,\xi}} L_j(s_i) - \kappa E^{22}_{\tau\zeta_{\frac{1}{H}}} L_j(s_i) + E^{26}_{\tau\zeta_{\frac{1}{H}}} A^{(1)}_{ij} + E^{25}_{\tau\zeta_{,\eta}} L_j(s_i) \\
\Pi_{13}^{\tau\zeta ij} =& E^{12}_{\tau\zeta_{,\eta}} L_j(s_i) + E^{25}_{\tau\zeta_{,\xi}} L_j(s_i) + E^{24}_{\tau\zeta_{\frac{1}{H}}} A^{(1)}_{ij} \\
\Pi_{21}^{\tau\zeta ij} =& E^{66}_{\tau\zeta_{,\xi}} L_j(s_i) + \kappa E^{66}_{\tau s_{\frac{1}{H}}} L_j(s_i) + E^{26}_{\tau\zeta_{\frac{1}{H}}} A^{(1)}_{ij} + E^{46}_{\tau\zeta_{,\eta}} L_j(s_i) \\
\Pi_{22}^{\tau\zeta ij} =& E^{66}_{\tau\zeta_{\frac{1}{H}}} A^{(1)}_{ij} + E^{36}_{\tau\zeta_{,\xi}} L_j(s_i) - \kappa E^{26}_{\tau\zeta_{\frac{1}{H}}} L_j(s_i) + E^{56}_{\tau\zeta_{,\eta}} L_j(s_i) \\
\Pi_{23}^{\tau\zeta ij} =& E^{16}_{\tau\zeta_{,\eta}} L_j(s_i) + E^{56}_{\tau\zeta_{,\xi}} L_j(s_i) + E^{46}_{\tau\zeta_{\frac{1}{H}}} L_j(s_i) \\
\Pi_{31}^{\tau\zeta ij} =& E^{44}_{\tau\zeta_{,\eta}} L_j(s_i) + E^{46}_{\tau\zeta_{,\xi}} L_j(s_i) + \kappa E^{46}_{\tau s_{\frac{1}{H}}} L_j(s_i) + E^{24}_{\tau\zeta_{\frac{1}{H}}} A^{(1)}_{ij} \\
\Pi_{32}^{\tau\zeta ij} =& E^{45}_{\tau\zeta_{,\eta}} L_j(s_i) + E^{34}_{\tau\zeta_{,\xi}} L_j(s_i) - \kappa E^{24}_{\tau\zeta_{\frac{1}{H}}} L_j(s_i) + E^{46}_{\tau\zeta_{\frac{1}{H}}} A^{(1)}_{ij} \\
\Pi_{33}^{\tau\zeta ij} =& E^{44}_{\tau s_{\frac{1}{H}}} A^{(1)}_{ij} + E^{45}_{\tau\zeta_{,\xi}} L_j(s_i) + E^{14}_{\tau\zeta_{,\eta}} L_j(s_i)
\end{aligned}
\tag{A.5}
$$

$$
\begin{aligned}
&M_{11}^{\tau\zeta ij} = E^{\rho}_{\tau\zeta H} L_j(s_i), \quad M_{12}^{\tau\zeta ij} = 0, \quad && M_{13}^{\tau\zeta ij} = 0 \\
&M_{21}^{\tau\zeta ij} = 0, && M_{22}^{\tau\zeta ij} = E^{\rho}_{\tau\zeta H} L_j(s_i), \quad M_{23}^{\tau\zeta ij} = 0 \\
&M_{31}^{\tau\zeta ij} = 0 && M_{32}^{\tau\zeta ij} = 0, \quad && M_{33}^{\tau\zeta ij} = E^{\rho}_{\tau\zeta H} L_j(s_i)
\end{aligned}
\tag{A.6}
$$

References

[1] J. N. Reddy. *Mechanics of laminated composite plates and shells: theory and analysis*. CRC Press, 2004.

[2] H. Elizalde, D. Cárdenas, J. C. Jáuregui-Correa, M. T. Piovan, and O. Probst. Vibrations of composite thin-walled beams with arbitrary curvature–a unified approach. *Thin-Walled Structures*, 147:106473, 2020.

[3] P. Chidamparam and A. W. Leissa. Vibrations of planar curved beams, rings, and arches. *Applied Mechanics Review*, 46(9):467–483, 1993.

[4] A. M. Yu and G. H. Nie. Explicit solutions for shearing and radial stresses in curved beams. *Mechanics Research Communications*, 32(3):323–331, 2005.

[5] C. N. Chen. Dqem analysis of in-plane vibration of curved beam structures. *Advances in Engineering Software*, 36(6):412–424, 2005.

[6] B. Kang, C. H. Riedel, and C. A. Tan. Free vibration analysis of planar curved beams by wave propagation. *Journal of Sound and Vibration*, 260(1):19–44, 2003.

[7] M. Hajianmaleki and M. S. Qatu. Vibrations of straight and curved composite beams: A review. *Composite Structures*, 100:218–232, 2013.

[8] I. Ecsedi and K. Dluhi. A linear model for the static and dynamic analysis of non-homogeneous curved beams. *Applied Mathematical Modelling*, 29(12):1211–1231, 2005.

[9] M. S. Qatu. In-plane vibration of slightly curved laminated composite beams. *Journal of Sound and Vibration*, 159(2):327–338, 1992.

[10] M. S. Qatu. Theories and analyses of thin and moderately thick laminated composite curved beams. *International Journal of Solids and Structures*, 30(20):2743–2756, 1993.

[11] M. Hajianmaleki and M. S. Qatu. Static and vibration analyses of thick, generally laminated deep curved beams with different boundary conditions. *Composites Part B: Engineering*, 43(4):1767–1775, 2012.

[12] A. A. Khdeir and J. N. Reddy. Free and forced vibration of cross-ply laminated composite shallow arches. *International Journal of Solids and Structures*, 34(10):1217–1234, 1997.

[13] A. Bhimaraddi. Generalized analysis of shear deformable rings and curved beams. *International Journal of Solids and Structures*, 24(4):363–373, 1988.

[14] A. Bhimaraddi, A. J. Carr, and P. J. Moss. Generalized finite element analysis of laminated curved beams with constant curvature. *Computers & Structures*, 31(3):309–317, 1989.

[15] H. Matsunaga. Free vibration and stability of laminated composite circular arches subjected to initial axial stress. *Journal of Sound and Vibration*, 271(3-5):651–670, 2004.

[16] S. R. Marur and T. Kant. Free vibration of higher-order sandwich and composite arches, part I: Formulation. *Journal of Sound and Vibration*, 310(1-2):91–109, 2008.

[17] X. Li and C. G. Soares. Spectral finite element analysis of in-plane free vibration of laminated composite shallow arches. *Composite Structures*, 132:484–494, 2015.

[18] P. Malekzadeh, A. R. Setoodeh, and E. Barmshouri. A hybrid layerwise and differential quadrature method for in-plane free vibration of laminated thick circular arches. *Journal of Sound and Vibration*, 315(1-2):212–225, 2008.

[19] M. Y. Yasin, H. M. Khalid, and M. S. Beg. Exact solution considering layerwise mechanics for laminated composite and sandwich curved beams of deep curvatures. *Composite Structures*, 244:112258, 2020.

[20] E. Carrera, G. Giunta, P. Nali, and M. Petrolo. Refined beam elements with arbitrary cross-section geometries. *Computers & Structures*, 88(5):283–293, 2010.

[21] E. Carrera and A. Pagani. Analysis of reinforced and thin-walled structures by multi-line refined 1D/beam models. *International Journal of Mechanical Sciences*, 75:278–287, 2013.

[22] E. Carrera, M. Filippi, P. K. R. Mahato, and A. Pagani. Accurate static response of single-and multi-cell laminated box beams. *Composite Structures*, 136:372–383, 2016.

[23] E. Carrera, A. G. De Miguel, and A. Pagani. Hierarchical theories of structures based on Legendre polynomial expansions with finite element applications. *International Journal of Mechanical Sciences*, 120:286–300, 2017.

[24] E. Carrera, M. Filippi, and E. Zappino. Free vibration analysis of rotating composite blades via Carrera Unified Formulation. *Composite Structures*, 106:317–325, 2013.

[25] M. Petrolo, I. Kaleel, G. De Pietro, and E. Carrera. Wave propagation in compact, thin-walled, layered, and heterogeneous structures using variable kinematics finite elements. *International Journal for Computational Methods in Engineering Science and Mechanics*, 19(3):207–220, 2018.

[26] Y. Yan, E. Carrera, A. Pagani, I. Kaleel, and A. G. de Miguel. Isogeometric analysis of 3D straight beam-type structures by Carrera Unified Formulation. *Applied Mathematical Modelling*, 79:768–792, 2020.

[27] E. Carrera, A. Pagani, and J. R. Banerjee. Linearized buckling analysis of isotropic and composite beam-columns by Carrera Unified Formulation and Dynamic Stiffness Method. *Mechanics of Advanced Materials and Structures*, 23(9):1092–1103, 2016.

[28] A. Pagani and E. Carrera. Large-deflection and post-buckling analyses of laminated composite beams by Carrera Unified Formulation. *Composite Structures*, 170:40–52, 2017.

[29] A. Pagani and E. Carrera. Unified formulation of geometrically nonlinear refined beam theories. *Mechanics of Advanced Materials and Structures*, 25(1):15–31, 2018.

[30] S. A. Sheikholeslami, M. M. Aghdam, E. Zappino, and E. Carrera. Application of refined beam elements to the coupled-field analysis of magnetostrictive microbeams. *Composites Part B: Engineering*, 115:14–20, 2017.

[31] F. Miglioretti and E. Carrera. Application of a refined multi-field beam model for the analysis of complex configurations. *Mechanics of Advanced Materials and Structures*, 22(1-2):52–66, 2015.

[32] E. Zappino, E. Carrera, S. Rowe, C. Mangeot, and H. Marques. Numerical analyses of piezoceramic actuators for high temperature applications. *Composite Structures*, 151:36–46, 2016.

[33] I. Kaleel, M. Petrolo, A. M. Waas, and E. Carrera. Micromechanical progressive failure analysis of fiber-reinforced composite using refined beam models. *Journal of Applied Mechanics*, 85(2), 2018.

[34] I. Kaleel, E. Carrera, and M. Petrolo. Progressive delamination of laminated composites via 1D models. *Composite Structures*, 235:111799, 2020.

[35] L. Qi, M. H. Nagaraj, E. Carrera, C. F. Gao, and M. Petrolo. Numerical analysis of disbonding in sandwich structures using 1D finite elements. *Composite Structures*, 252:112717, 2020.

[36] C. Liu, B. Liu, L. Zhao, Y. Xing, C. Ma, and H. Li. A differential quadrature hierarchical finite element method and its applications to vibration and bending of Mindlin plates with curvilinear domains. *International Journal for Numerical Methods in Engineering*, 109(2):174–197, 2017.

[37] B. Liu, C. Liu, S. Lu, Y. Wu, Y. Xing, and A. J. M. Ferreira. A differential quadrature hierarchical finite element method using Fekete points for triangles and tetrahedrons and its applications to structural vibration. *Computer Methods in Applied Mechanics and Engineering*, 349:798–838, 2019.

[38] I. Babuska, B. A. Szabo, and I. N. Katz. The p-version of the finite element method. *SIAM Journal on Numerical Analysis*, 18(3):515–545, 1981.

[39] Y. Yan, A. Pagani, and E. Carrera. Exact solutions for free vibration analysis of laminated, box and sandwich beams by refined layer-wise theory. *Composite Structures*, 175:28–45, 2017.

[40] A. Pagani, Y. Yan, and E. Carrera. Exact solutions for static analysis of laminated, box and sandwich beams by refined layer-wise theory. *Composites Part B: Engineering*, 131:62–75, 2017.

[41] Y. Yan, A. Pagani, E. Carrera, and Q. W. Ren. Exact solutions for the macro-, meso- and micro-scale analysis of composite laminates and sandwich structures. *Journal of Composite Materials*, 52(22):3109–3124, 2018.

[42] G. De Pietro, A. G. De Miguel, E. Carrera, G. Giunta, S. Belouettar, and A. Pagani. Strong and weak form solutions of curved beams via Carreras unified formulation. *Mechanics of Advanced Materials and Structures*, 27(15):1342–1353, 2020.

[43] A. G. De Miguel, G. De Pietro, E. Carrera, G. Giunta, and A. Pagani. Locking-free curved elements with refined kinematics for the analysis of composite structures. *Computer Methods in Applied Mechanics and Engineering*, 337:481–500, 2018.

[44] A. Pagani, E. Carrera, and A. J. M. Ferreira. Higher-order theories and radial basis functions applied to free vibration analysis of thin-walled beams. *Mechanics of Advanced Materials and Structures*, 23(9):1080–1091, 2016.

[45] Y. Yan, E. Carrera, A. G. Miguel, A. Pagani, and Q. W. Ren. Meshless analysis of metallic and composite beam structures by advanced hierarchical models with layer-wise capabilities. *Composite Structures*, 200:380-395, 2018.

[46] S. O. Ojo and P. M. Weaver. 3D static analysis of patched composite laminates using a multidomain differential quadrature method. *Composite Structures*, 229:111389, 2019.

[47] S. O. Ojo, M. Patni, and P. M. Weaver. Comparison of weak and strong formulations for 3D stress predictions of composite beam structures. *International Journal of Solids and Structures*, 178:145–166, 2019.

[48] R. Bellman, B. G. Kashef, and J. Casti. Differential quadrature: a technique for the rapid solution of nonlinear partial differential equations. *Journal of Computational Physics*, 10(1):40–52, 1972.

[49] C. Shu and B. E. Richards. Application of generalized differential quadrature to solve two-dimensional incompressible Navier-Stokes equations. *International Journal for Numerical Methods in Fluids*, 15(7):791–798, 1992.

[50] Z. Zong and Y. Zhang. *Advanced differential quadrature methods*. CRC Press, 2009.

[51] C. Shu. *Differential quadrature and its application in engineering*. Springer Science & Business Media, 2012.

[52] H. Zhong and T. Yu. A weak form quadrature element method for plane elasticity problems. *Applied Mathematical Modelling*, 33(10):3801–3814, 2009.

[53] H. Zhong and Y. Wang. Weak form quadrature element analysis of Bickford beams. *European Journal of Mechanics-A/Solids*, 29(5):851–858, 2010.